UCB-NE-4217

RADIONUCLIDE TRANSPORT IN DISTURBED ZONE BETWEEN ENGINEERED AND NATURAL BARRIERS OF DEEP GEOLOGIC DISPOSAL OF HIGH-LEVEL RADIOACTIVE WASTES

J. Ahn, P. L. Chambré, B. Light, D. Roberts, and J. Verbeke

Department of Nuclear Engineering
University of California
Berkeley, California 94720

August 1996

The authors invite comments and would appreciate being notified of any errors in the report.

Joonhong Ahn
Department of Nuclear Engineering
University of California
Berkeley, CA 94720
USA

ahn@nuc.berkeley.edu

TABLE OF CONTENTS

TABLE OF CONTENTS.....iii

LIST OF FIGURES.....v

LIST OF TABLES.....vi

ACKNOWLEDGMENTS.....vii

1. INTRODUCTION AND SUMMARY

1.1 Background.....1-1

1.2 Objective of This Study.....1-1

1.3 Summary of the Results.....1-1

1.4 Conclusions.....1-2

1.5 Future Plan.....1-3

1.6 References for Chapter 1.....1-3

2. INTEGRATED PERFORMANCE ANALYSIS FOR GEOLOGIC REPOSITORY IN WATER-SATURATED MEDIA

2.1 Introduction.....2-1

2.2 Mathematical Model for Transport in Natural Barrier.....2-1
2.2.1 Assumptions and Geometry.....2-1
2.2.2 Governing Equations and Side Conditions.....2-3
2.2.3 Analytical Solutions.....2-4

2.3 Mathematical Models for Source Terms.....2-5
2.3.1 Assumptions and Governing Equations.....2-5
2.3.2 Side Conditions.....2-7
2.3.3 Determination of Inner Boundary Conditions.....2-8
2.3.4 Analytical Solutions.....2-10
2.3.5 Limitations of the Source Term Model.....2-11

2.4 Numerical Results and Discussions.....2-12
2.4.1 Input Data.....2-12
2.4.2 Computer Code.....2-14
2.4.3 Inner Boundary Conditions.....2-15
2.4.4 Radionuclide Release from the EBS.....2-15
2.4.5 Radionuclide Transport in the NBS.....2-17
2.4.6 Effect of Minor Actinides Recovery from HLW.....2-18

2.5 Conclusions.....2-19

2.6 References for Chapter 2 2-19

3. MASS TRANSPORT IN DISTURBED ZONE

3.1 Introduction and Background.....3-1

3.2 Mathematical Model.....3-2
3.2.1 Governing Equations.....3-2
3.2.2 Analytical Solutions.....3-4

3.3 Numerical Results and Discussions.....3-5
3.3.1 Input Data.....3-5
3.3.2 Numerical Results.....3-8

3.4 Concluding Remarks.....3-11

3.5 References for Chapter 3 3-12

3.A Sorption Ratio Measurement.....3-12
3.A.1 Materials.....3-12
3.A.2 Procedure.....3-12
3.A.3 Results.....3-13
3.A.4 References for Appendix 3-13

4. BENTONITE RE-DISTRIBUTION IN DISTURBED ZONE

4.1 Description of Swelling in a Microscopic Level 4-1
4.1.1 Basic Structural Unit.....4-1
4.1.2 The Electrical Charge on a Bentonite Particle 4-2
4.1.3 The Electrical Double Layer: General Observation 4-2
4.1.4 Effective Stress 4-6

4.2 Mathematical Model for Swelling.....4-7
4.2.1 Governing Equations.....4-7
4.2.2 Bentonite Saturated with Water.....4-10

4.3 References for Chapter 4 4-12

LIST OF FIGURES

Figure 2.1 Conceptual configuration of parallel fractures in the host rock. Radionuclides released from the engineered barriers enter from the left.....2-2

Figure 2.2 Conceptual configuration of the engineered barriers. The dimensions for the original cylindrical geometry are from Ref. [9].....2-6

Figure 2.3 Radiological hazards resulting from ingestion of radionuclides contained in the fraction of the waste solid that alters every year. For the left figure, the waste solid is assumed to alter for 40,000 years at a constant rate. For the right figure, 4 million year is assumed. 2-16

Figure 2.4 Radiological hazards of radionuclides released at the surface of the bentonite region for T_L = 40,000 and 4 million years. 2-16

Figure 2.5 Radiological hazards of radionuclides in the natural barrier. Transport distance through the fractures is 10 m (left) or 100 m (right). The leach time is assumed to be 40,000 yr.....2-17

Figure 2.6 Effect of recovering Cm, Am, and Np from the waste solid. 90% (left) or 99% (right) recovery is assumed. No recovery case is shown in the left graph of Figure 2.5. The leach time is 40,000 yr. Transport distance from the engineered barrier surface is 10 m.....2-18

Figure 3.1 Conceptual transport path around EBS.....3-1

Figure 3.2 The engineered barrier intersected by planar fractures.....3-2

Figure 3.3 Sherwood Number as a Function of Peclet Number [2].....3-7

Figure 3.4 Experimental results for sorption distribution coefficients (Kd) of americium and neptunium with loosely compacted bentonite [3].....3-8

Figure 3.5 Normalized mass flux at the tip of the extruding bentonite in the fracture, as a function of Fourier number.....3-8

Figure 3.6 Concentration isopleths for 243Am and 237Np for the oxidizing condition.....3-9

Figure 3.7 Reduction Factor vs. Thiele Modulus.....3-10

Figure 3.8 Reduction factor as a function of Sherwood number. 3-11

Figure 3.A.1 Sorption cell configuration.....3-13

Figure 4.1 Basic units of silica (left) and gibbsite (right) [1].....4-1

Figure 4.2 Two-dimensional views of silica and gibbsite.....4-2

Figure 4.3 The structure of pyrophyllite. (a) Atomic structure. (b) Symbolic structure 4-3

Figure 4.4 Particle surface with exchangeable ions. Surface of dry montmorillonite 4-3

Figure 4.5 (a) A hypothetical model for a multilayer configuration of clay-water interphase. (b) Decay of the surface potential in the interphase region

(clay surface is represented by the basal oxygens and the tetrahedral cations.) ……4-4
Figure 4.6 Energies of repulsion, attraction, and net curves of interaction for parallel plates……4-5
Figure 4.7 Forces between particles……4-7
Figure 4.8 Variation of void ratio in relation to swelling pressure……4-9
Figure 4.9 Idealized void ratio-effective stress relationships for a compressible soil ……4-9
Figure 4.10 Variation of hydraulic conductivity with void ratio for some saturated soils……4-11

LIST OF TABLES

Table 2.1 Assumed parameter values……2-12
Table 2.2 Input data for radionuclides and determined boundary conditions. ……2-13
Table 2.3 Assumed elemental parameters ……2-14
Table 3.1 Parameter values applied in the calculations……3-6
Table 3.2 Parameter values assigned for each radionuclide……3-7

ACKNOWLEDGMENTS

The research reported herein was supported by JGC Corporation, Japan, as part of a study on the geologic disposal system for the high-level radioactive waste, organized by the Central Research Institute for Electrical Power Industry (CRIEPI), Japan, and Tokyo Electric Power Industry Co., Japan.

CHAPTER
ONE

INTRODUCTION AND SUMMARY

1.1 BACKGROUND

In the assessment for the long-term performance of deep geologic repositories for high-level radioactive wastes (HLW), the main task is the analysis for transport of long-lived radionuclides such as actinides, their daughters, ^{99}Tc, ^{129}I, and ^{135}Cs, through the engineered and the natural barriers.

Recent repository performance studies [1,2] show that, due to their extremely low solubilities in reducing geochemical environments, actinides will precipitate at the location where they are released from the waste solid. The radionuclide concentration in groundwater contacting the precipitate of the species is limited by its solubility as long as the precipitate exists. Consequently, only a small amount of actinides can actually be released from the engineered barriers (EBS) to the surrounding geologic formations, and to the biosphere.

In the host rock adjacent to the engineered barriers, disturbance will be introduced during the construction and waste-emplacement period. Geochemical, hydrological, and rock-mechanical properties would be different from those of undisturbed host rock. The disturbed region is important because this region directly affects the hydrological and geochemical environment of the engineered barriers, and might behave as a barrier through which radioactivities released from the engineered barriers might be weakened further.

1.2 OBJECTIVE OF THIS STUDY

The goal of this project is to establish theoretical background for distinguishing the disturbed zone from the undisturbed natural barrier, and to investigate radionuclide transport in the disturbed region.

To accomplish this goal, in FY95, we set the following three tasks:

• The first task (see Chapter 2) is to show that, within a relatively short transport distance through the natural barrier, the total hazard is significantly reduced. This task will be carried out by using a transport model without the disturbed region, where the release from the engineered barriers is directly used as an source term for the transport in the host rock.

• The second task (see Chapter 3) is to show that significant reduction in radiological toxicity actually occurs in the disturbed host-rock region contacting the engineered barriers. The disturbed region is temporarily considered as the region, where swollen bentonite exists in fractures of highly fractured host rock, and

• The third task is (see Chapter 4) is to establish a mathematical formulation for the bentonite re-distribution, which determines the fundamental environment of the disturbed region.

1.3 SUMMARY OF THE RESULTS

Chapter 2

The time-dependent total radiological toxicity of radionuclides released from the waste glass logs is calculated at the surface of the engineered barriers and at the points in the natural barrier 10

and 100 m downstream from the engineered barriers. An integrated mathematical model for release and transport of radionuclides in the engineered barriers and subsequently in the natural barrier has been developed.

The major hazard contributors are ^{243}Am and ^{241}Am in the waste form, ^{239}Pu, ^{229}Th, and ^{243}Am at the surface of the engineered barriers, ^{223}Ra, ^{231}Pa, and ^{227}Ac at 10 m location from the engineered barriers, and ^{99}Tc, ^{223}Ra, and ^{225}Ra at 100 m location.

With a distance of 100 m through the natural barrier, four orders of magnitude reduction in the total hazard is observed. Thus, the importance of the region in the vicinity of the engineered barriers in the context of the repository performance can be pointed out.

Since the major contributors in the host rock are the daughters of minor actinides, recovery of minor actinides reduces the total hazard in the natural barrier. However, the radiological hazard would be reduced much more effectively by the 100-m thick geologic formation around the repository than by even a 99% recovery of the actinides.

Chapter 3

Radionuclide transport through the disturbed zone around the engineered barriers is analyzed, based on a configuration with parallel fractures, intersecting the engineered barriers and filled with bentonite extruding from the EBS to the intersecting fractures. Readily available experimental results for sorption distribution coefficients of Am and Np for bentonite in a simulated rock fracture are utilized for the calculation. The radionuclide reduction factor is defined as the ratio of the total mass of the radionuclide leaving the disturbed region to that entering the region. The distance of the bentonite extrusion into fractures is assumed to be constant and known.

The numerical results show that, for americium, plutonium, and neptunium, if the environment is reducing, the disturbed region plays as a very effective barrier; the radioactivities of these nuclides will decay to negligible levels. Only uranium isotopes and their daughters can survive, and will be released to the circulating groundwater system in the undisturbed host rock, because of their long half-lives.

Chapter 4

Microscopic mechanisms of bentonite swelling are studied and summarized by literature survey. Neither the electrical double layer theory [3] nor the recently-proposed hydration theory [4] gives complete mechanistic explanation for clay swelling phenomena. On the other hand, macroscopic behaviour of clay and soils have been analyzed successfully by consolidation theory, which was established in a series of studies by Terzaghi since the 1920's [5]. Here, we follow the consolidation theory, without being involved in microscopic details of mechanisms of swelling, and establish a mathematical model for redistribution of bentonite in the disturbed region.

1.4 CONCLUSIONS

• If we define the disturbed region as the region enveloped by the tips of the extruding bentonite in fractures, most of the radioactivity initially contained in the waste glass log will decay to negligible levels within the engineered barriers and the disturbed region. Only uranium isotopes, their daughters, and weakly-sorbing Tc could come out of the disturbed region, because of their extremely long half-lives.

• Thus, the role of the disturbed region is more important in the context of the performance of the geologic repository than that of the far-field region, where major uncertainties are introduced.

• We establish the mathematical formulation for swelling of bentonite.

1.5 FUTURE PLAN

An analysis for bentonite redistribution will be performed, based on the mathematical model we develop herein, the result of which gives the extent of the disturbed zone.

We will make quantitative evaluation based on the mathematical model, and determine which parameters are essential for the swelling of bentonite. We will propose experimental studies, where the essential bentonite properties are measured in such a way that they can be utilized for further quantitative analysis of the mathematical model.

Geochemical analysis will follow, which determines the geochemical environment in the disturbed region. We will consider how the disturbed region affects the EBS environment. After we establish the geochemistry for the EBS and the disturbed region, we will study radionuclide transport in the repository region.

1.6 REFERENCES FOR CHAPTER 1

[1] Power Reactor and Nuclear Fuel Development Corporation, *Technical Report on Research and Development for Geological Disposal of High-Level Radioactive Wastes,* PNC TN 1410 92-08 (1992).

[2] NAGRA, Kristallin-I: Safety Assessment Report, Tech. Rep. 93-22E, Nagra, Wettingen, Switzerland (1994).

[3] J. K. Mitchell, *Fundamentals of Soil Behaviour,* 2nd ed., Wiley, New York (1993).

[4] P. F. Low, Interparticle Forces in Clay Suspensions: Flocculation, Viscous Flow and Swelling, *Proc. 1989 Clay Min. Soc. Workshop on Rheology of Clay/Water Systems* (1992).

[5] For example, K. Terzaghi, The Influence of Elasticity and permeability on the Swelling of Two-Phase Systems. In J. Alexander (ed.) *Colloid Chemistry,* Vol. III, Chemical Catalog Co., New York, pp. 65-88 (1931).

CHAPTER
TWO

INTEGRATED PERFORMANCE ANALYSIS FOR GEOLOGIC REPOSITORY IN WATER-SATURATED MEDIA

2.1 INTRODUCTION

Presented in this chapter is a mathematical model for radionuclide transport through the water-saturated natural barrier integrated with the source term model, where precipitation at the waste-solid alteration location and subsequent transport of radionuclides in the engineered barriers are considered. Multiple-member decay chains are taken into account both for the transport model in the natural barrier and for the source term analysis. For the transport of radionuclides in the natural barrier, the parallel planar fracture model is adopted, for which the analytical solution has been obtained elsewhere [1]. For the source term, new analytical solutions are obtained. A computer code, Transport To Biopshere (TTB), has been developed, based on these analytical solutions. Transport of radionuclides can now be analyzed with the computer code from the release from the waste solid to the exit of the geosphere.

The model developed here takes into account radioactive decay for mechanisms that decrease the amount of radionuclides arriving a certain location in the natural barrier.

Utilizing the present model, we will evaluate quantitatively which radionuclides will significantly contribute to the radiological toxicity resulting from ingestion of radionuclides reaching a certain point located between the waste-solid surface and the exit of the natural barrier (see Sections 2.4.4 and 2.4.5.).

The effects of recovering actinides from the HLW on the performance of the geologic repository have been discussed by many researchers. One of the important consequences of the previous repository performance studies is that, because most actinides would precipitate in the vicinity of the original waste solid locations due to their extremely low solubilities, the effects of actinide recovery would be apparent only if they are recovered with an unrealistically good recovery ratio [2]. In this chapter, the effect of actinide recovery will also be investigated with the integrated model (see Section 2.4.6.).

2.2 MATHEMATICAL MODEL FOR TRANSPORT IN NATURAL BARRIER

2.2.1 Assumptions and Geometry

Consider a rock matrix containing multiple parallel planar fractures of width $2b$, with a spacing of $2a$, situated in a water-saturated porous rock of porosity ε_p (See Figure 2.1). We include the following physical and chemical phenomena in the sub-model for transport in the natural barrier: (a) advection in the fractures, (b) longitudinal hydrodynamic dispersion in the direction of the fracture axis in the fractures, (c) molecular diffusion in the rock matrix, (d) sorption onto the fracture surfaces, (e) sorption in the rock matrix, and (f) a radioactive decay chain of arbitrary length.

The velocity v and the longitudinal hydrodynamic dispersion coefficient D^L are assumed to be constant with time and uniform in space. They are also assumed to be common for all radionuclides, since the hydrodynamic dispersion is determined mainly by the geometry of the contaminant transport paths.

Molecular diffusion of radionuclides from water flowing in the fractures into stationary water in the pores of the rock matrix is an important retardation mechanism. In the present study, we use an intrinsic diffusion coefficient, $D^I_{e(k)}$, for radionuclide k of element e in the rock defined as

$$D^I_{e(k)} = \varepsilon_p \tau_p D_{e(k)}. \tag{2.1}$$

where τ is the tortuosity correction factor for the host rock, and $D_{e(k)}$ the diffusion coefficient in free water.

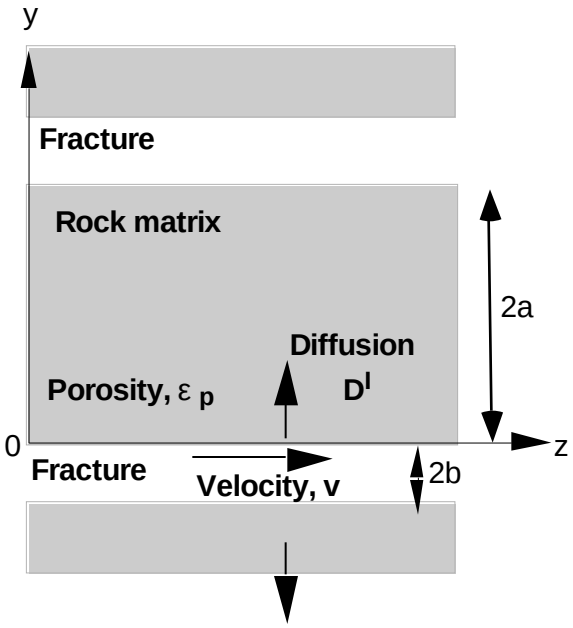

Figure 2.1 Conceptual configuration of parallel fractures in the host rock. Radionuclides released from the engineered barriers enter from the left.

Sorption by the materials filling the fractures and sorption within the rock matrix are considered separately because of the possibility of differing chemical properties in the fracture and in the rock matrix. For the porous rock matrix, we define the capacity factor for radionuclide k of element e as

$$\alpha_{e(k)} = \varepsilon_p + \rho_p (1 - \varepsilon_p) K^e_{dp}, \tag{2.2}$$

where ρ [kg/m^3] is the density of the rock matrix, and K^e_{dp} [m^3/kg] the sorption distribution coefficient of element e for the rock matrix. The retardation coefficient, $R_{e(k)}$, for advection and longitudinal dispersion in the fractures can be defined as

$$R_{e(k)} = 1 + \frac{\rho_f (1 - \varepsilon_f) K^e_{df}}{\varepsilon_f}, \tag{2.3}$$

where ρ and ε are the density and the porosity of the material filling the fractures. K_{df}^{e} [m^3/kg] is the sorption distribution coefficient of element e for the material filling the fractures.

We make the following assumptions relating to the geometry and hydraulic properties of the system [3]. By the assumptions that the fracture aperture, $2b$, is much smaller than the scale considered in the water-flow (z) direction, and that diffusion and dispersion across the fracture aperture assure complete mixing, mass transport along the fracture can be represented in a one-dimensional flow field. Furthermore, by assuming that the permeability of the porous rock is very low and transport in the rock will be mainly by molecular diffusion, and that transport along the fracture is much faster than transport in the rock, we can take the direction of mass flux in the rock matrix to be perpendicular to the fracture plane.

We can simplify the basically two-dimensional system into two one-dimensional systems: one for the concentration of radionuclides in water in the fracture and one for their concentration in water in the rock pores. The coupling of two one-dimensional systems is provided by the continuity of fluxes and concentrations along the rock/fracture interface.

2.2.2 Governing Equations and Side Conditions

With the above assumptions, the basic radionuclide transport equations for the concentration in the fracture, $C_k(z, t)$, and in the pores of the rock matrix, $C_k^P(y, t; z)$ are

$$R_{e(k)}\frac{\partial C_k}{\partial t} + v\frac{\partial C_k}{\partial z} - D^L\frac{\partial^2 C_k}{\partial^2 z} - \frac{D_{e(k)}^I}{b}\frac{\partial C_k^P}{\partial y}\bigg|_{y=0} + R_{e(k)}\lambda_k C_k - R_{e(k-1)}\lambda_{k-1}C_{k-1} = 0, \quad t > 0, z > 0, \tag{2.4}$$

and

$$\alpha_{e(k)}\frac{\partial C_k^P}{\partial t} = D_{e(k)}^I\frac{\partial^2 C_k^P}{\partial y^2} - \alpha_{e(k)}\lambda_k C_k^P + \alpha_{e(k-1)}\lambda_{k-1}C_{k-1}^P, t > 0, 0 < y < a, z > 0. \tag{2.5}$$

The initial and boundary conditions are:

$$C_k(z, 0) = 0, z > 0, \tag{2.6}$$

$$C_k^P(y, 0; z) = 0, 0 < y < a, z > 0, \tag{2.7}$$

$$\varepsilon\left[v_I C_k(0, t) - D_I^L\frac{\partial C_k}{\partial z}\bigg|_{z=0}\right] = \frac{Q_k(t)}{A}, t > 0, \tag{2.8}$$

$$C_k(\infty, t) = 0, t > 0, \tag{2.9}$$

$$C_k^P(0, t; z) = C_k(z, t), t > 0, z > 0, \tag{2.10}$$

$$\frac{\partial C_k^P}{\partial y}\bigg|_{y=a} = 0, t > 0, z > 0. \tag{2.11}$$

The constants v_I and D_I^L in (2.8) will be set equal to v and D^L, but may be set to other values if required. The time dependent function, $Q_k(t)$, in (2.8) is the flux of radionuclide k from the engineered barriers, and is obtained later by considering the mass transport in the engineered barriers with help of (2.55).

The factor A [1] in (2.8) is determined by the repository configuration. With the repository dimensions of $L_R \times L_R$ [m^2], the number, n_w, of the waste canisters placed in the repository, the number, n_f, of the fractures intersecting the repository, and the surface area of an equivalent spherical EBS (see Figure 2.2), $S_2 = 4\pi r_t$, the factor is expressed as

$$A = \frac{2bL_R n}{n_w S_2}. \tag{2.12}$$

2.2.3 Analytical Solutions

The Laplace-transformed analytical solutions for this problem have been obtained elsewhere [1], and are written here for the rock:

$$\tilde{C}_k^P(y, z, s) = \sum_{m=1}^{k} \tilde{C}_m(z; s) w_{mk}(y, s), \tag{2.13}$$

where for $m = k$,
$$w_{kk}(y, s) = \frac{\cosh\left[\zeta_k(s)(a - y)\right]}{\cosh\left[\zeta_k(s)a\right]}, \tag{2.14}$$

and for $m < k$,
$$w_{mk}(y, s) = \left(\prod_{n=m}^{k-1} \frac{\alpha_{e(n)}\lambda_n}{D^I_{e(n+1)}}\right) \sum_{n=m}^{k} \frac{w_{nn}(y, s)}{\prod_{\substack{\ell=m \\ \ell \neq n}}^{k} \left[\zeta_\ell^2(s) - \zeta_n^2(s)\right]}, \tag{2.15}$$

with
$$\zeta_m(s) = \sqrt{\frac{(s + \lambda_m)\alpha_{e(m)}}{D^I_{e(m)}}}. \tag{2.16}$$

where s is a complex-valued Laplace-transform variable, and ~ denotes a Laplace-transform.

In the fracture,

$$\tilde{C}_k(z; s) = \sum_{m=1}^{k} u_{mk}(s) a_m(s) \exp\left[-b_m(s) z\right], \tag{2.17}$$

where

$$b_m(s) = \frac{v}{2D^L}\left\{-1 + \sqrt{1 + \frac{4D^L g_m(s)}{v^2}}\right\}, \tag{2.18}$$

$$g_m(s) = R_{e(m)}(s + \lambda_m) + \frac{D^I_{e(m)}}{b}\zeta_m(s)\tanh\left[\zeta_m(s)a\right], \tag{2.19}$$

$$\left[g_k(s) - g_m(s)\right] u_{mk}(s) = R_{e(k-1)}\lambda_{k-1} u_{m,k-1}(s) + \sum_{n=m}^{k-1} B_{nk}(s) u_{mn}(s), \tag{2.20}$$

with
$$u_{kk}(s) = 1, \tag{2.21}$$

$$B_{nk}(s) = -\frac{D^I_{e(k)}}{b}\left(\prod_{i=n}^{k-1}\frac{\alpha_{e(i)}\lambda_i}{D^I_{e(i+1)}}\right)\sum_{i=n}^{k}\frac{\zeta_i(s)\tanh\left[\zeta_i(s)a\right]}{\prod_{\substack{j=n\\ j\neq i}}^{k}\left[\zeta^2_j(s)-\zeta^2_i(s)\right]}, \tag{2.22}$$

$$a_m(s) = \frac{1}{v_I + D^L_I b_m(s)}\sum_{n=1}^{m} v_{nm}(s)\frac{\tilde{Q}_n(s)}{\varepsilon_I A}, \tag{2.23}$$

and
$$v_{nm}(s) = -\sum_{j=n}^{m-1} u_{jm}(s)v_{nj}(s) \qquad \text{for } m > n \tag{2.24}$$

with
$$v_{mm}(s) = 1. \tag{2.25}$$

The mass flux of radionuclide k in the fracture at a distance z from the fracture entrance can be obtained by

$$\tilde{J}_k(z; s) = v\tilde{C}_k(z; s) - D^L\frac{d\tilde{C}_k}{dz} \tag{2.26}$$

If we set $v_I = v$ and $D^L_I = D^L$, from eq. (2.17), (2.23), and (2.26), we obtain

$$\tilde{J}_k(z; s) = \sum_{m=1}^{k}\sum_{n=1}^{m} u_{mk}(s)v_{nm}(s)\exp\left[-b_m(s)z\right]\frac{\tilde{Q}_n(s)}{\varepsilon_I A}. \tag{2.27}$$

These Laplace-transformed quantities will be inverted numerically (see Section 2.4.2).

2.3 MATHEMATICAL MODELS FOR SOURCE TERMS

2.3.1 Assumptions and Governing Equations

To evaluate concentrations of radionuclides in the host rock, given by their Laplace transforms, (2.13), (2.17), and the transformed mass flux, (2.27), we need to determine a Laplace transform of $Q_k(t)$, the mass flux at the entrance to the far-field. To establish the mathematical model for evaluating $Q_k(t)$, we start with the review of the engineered barriers.

In designs proposed for future HLW repositories in water-saturated geologic formations [4,5], a metal container and a bentonite-filled buffer region exist between the waste solid and the host rock. In the present study, the region between the waste solid and the surrounding rock formation is simplified as a single uniform porous medium, whose physical and chemical properties are represented by those of bentonite. This region is called the bentonite region herein.

Bentonite is expected to have a hydraulic conductivity more than three orders of magnitude smaller than that of the surrounding host rock [4]. Therefore, we assume that radionuclides are transported only by molecular diffusion through the stationary water in the pores of the bentonite region. Because molecular diffusion is constrained in tortuous paths in the pores, the diffusion coefficient, $D_{e(k)}$ [m^2/yr], in the bentonite region for element e becomes smaller than that in free water, $D_{e(k)}$, by the tortuosity correction factor τ. Here, subscript $e(k)$ indicates that the k-th member nuclide in a decay chain is an isotope of element e.

To simplify, we consider equivalent spheres for the waste solid and the bentonite region, which have the same interfacial areas (see Figure 2.2).

The governing equations for the radionuclide concentrations in the water phase in the bentonite region are written as

$$K_{e(1)}\frac{\partial N_1}{\partial t} + \lambda_1 K_{e(1)} N_1 = D_{e(1)}\frac{1}{r^2}\frac{\partial}{\partial r}\left(r^2\frac{\partial N_1}{\partial r}\right),$$

$$K_{e(2)}\frac{\partial N_2}{\partial t} + \lambda_2 K_{e(2)} N_2 = D_{e(2)}\frac{1}{r^2}\frac{\partial}{\partial r}\left(r^2\frac{\partial N_2}{\partial r}\right) + \lambda_1 K_{e(1)} N_1, \qquad (2.28)$$

$$\vdots \qquad \vdots$$

$$K_{e(i)}\frac{\partial N_i}{\partial t} + \lambda_i K_{e(i)} N_i = D_{e(i)}\frac{1}{r^2}\frac{\partial}{\partial r}\left(r^2\frac{\partial N_i}{\partial r}\right) + \lambda_{i-1} K_{e(i-1)} N_{i-1},$$

$$t > 0, \; r_1 < r < r_2$$

where $N_k(r, t)$ [mol/m^3] is the concentration of the k-th member radionuclide in a decay chain of length i, r [m] the distance from the center of the waste solid, t [yr] time, $K_{e(k)}$ the retardation coefficient [1] for element e, and λ_k [yr^{-1}] the decay constant of radionuclide k. Isotopes of element e have identical retardation and diffusion coefficients. r_1 and r_2 [m] are the radii of the equivalent-sphere waste solid and bentonite region, respectively.

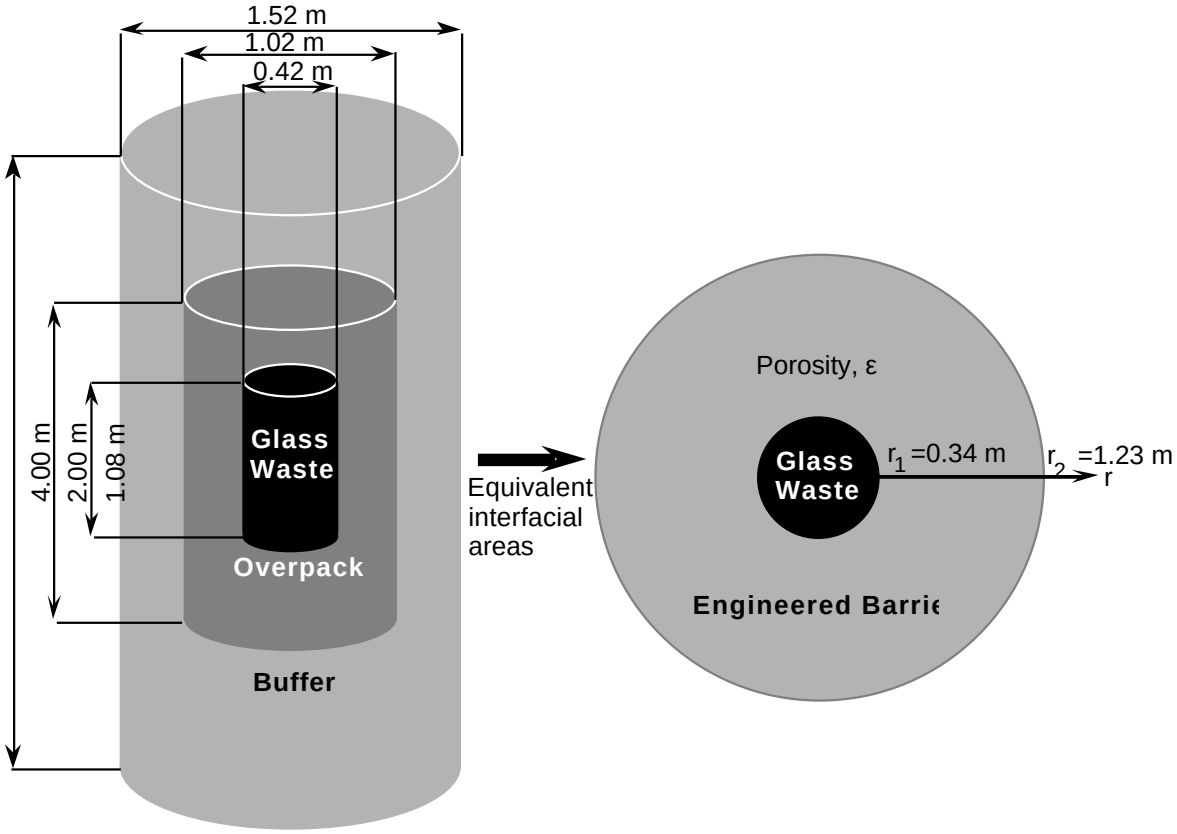

Figure 2.2 Conceptual configuration of the engineered barriers. The dimensions for the original cylindrical geometry are from Ref. [6].

We assume that local sorption equilibrium between radionuclide concentrations in the water and in the solid of the bentonite region is established. Sorption is also assumed to be a reversible reaction with a constant distribution coefficient, K_d^e [m^3/kg]. Sorption apparently retards movement of radionuclides by molecular diffusion. The retardation coefficient, $K_{e(k)}$, is defined as:

$$K_{e(k)} = 1 + \frac{\rho(1 - \varepsilon)}{\varepsilon} K_d^e \tag{2.29}$$

where ρ [kg/m^3] and ε are the density and the porosity of the bentonite, respectively. Here, K_d^e is determined for each element *e*. $K_{e(k)}$ represents the retardation coefficient of the *k*-th radionuclide, which is element *e*, in the radioactive decay chain.

2.3.2 Side Conditions

The governing equations (2.28) are solved, subject to the following initial and boundary conditions. There is no radionuclide in the bentonite region initially. Hence, the initial condition is written as

$$N_k(r,0) = 0, r_1 < r < r_2, \; k = 1, 2, \ldots, i, \tag{2.30}$$

At the outer boundary, $r = r_2$, we apply

$$N_k(r_2, t) = 0, t > 0, \; k = 1, 2, \ldots, i. \tag{2.31}$$

This boundary condition gives a steeper concentration gradient in the bentonite region, resulting in a greater release rate to the host rock, than reality.

On the waste-solid surface, $r = r_1$, there would be precipitates of radionuclide *k*, if its solubility is so low or the release from the waste solid by alteration of the waste solid matrix is so much that all the radionuclides released cannot dissolve into the water phase.

We consider two extreme cases that are described below.

In one case, we assume that the precipitate of radionuclide *k* covers the entire waste-solid surface, and that the precipitate thickness increases or decreases uniformly. Then, we have at the waste-solid surface at $r = r_1$,

$$N_k(r_1, t) = \gamma_k(t) N_e^* \{h(t) - h(t - t_k^*)\}, t > 0, k = 1, 2, \ldots, i, \tag{2.32}$$

where $h(\bullet)$ is a Heaviside step function, N_e^* [mol/m^3] the solubility of element *e* and $\gamma_k(t)$ the fraction of radionuclide *k* in the precipitate of element *e* , defined as

$$\gamma_k(t) = \frac{P_k(t)}{\sum P_k(t)}, \tag{2.33}$$

where $P_k(t)$ [mol] is the amount of precipitate *k* at $r = r_1$. The summation in the denominator is taken over all the isotopes of element *e*. t_k^* [yr] is the time when the precipitate disappears, which can be determined by the analysis shown in Section 2.3.3.

In the other case, we assume that there is no precipitate of radionuclide *k* at the surface of the waste solid. Then, we have at the waste-solid surface at $r = r_1$,

$$- D_{e(k)} \varepsilon \frac{\partial N_k}{\partial r}\bigg|_{r = r_1} = m_k(t) \{h(t) - h(t - T_L)\}, t > 0, k = 1, 2, \ldots, i, \tag{2.34}$$

where $m_k(t)$ [mol/m^2·yr] is the congruent release rate of radionuclide k. T_L [yr] is the leach time of the waste solid, which is the time period between the beginning and the end of the waste solid alteration.

The boundary conditions, (2.32) and (2.34), can be symbolically represented by

$$-(1-\sigma_k)D_{e(k)}\varepsilon\frac{\partial N_k}{\partial r}\bigg|_{r=r_1}+\sigma_k N_k(r_1,t)=\begin{cases}\gamma_k(t)\,N_e^*\{h(t)-h(t-t_k^*)\}, & \text{for } \sigma_k=1\\ m_k(t)\{h(t)-h(t-T_L)\}, & \text{for } \sigma_k=0\end{cases} \quad t>0,\ k=1,2,\ldots,i \tag{2.35}$$

where σ_k is a constant whose value is either 1 or 0, corresponding to the boundary conditions (2.32) and (2.34), respectively. Hereafter, we denote symbolically the right-hand side of (2.35) as $\psi_k(t)$:

$$\psi_k(t)=(1-\sigma_k)m_k(t)\{h(t)-h(t-T_L)\}+\sigma_k\gamma_k(t)\,N_e^*\{h(t)-h(t-t_k^*)\},\ t>0,\ k=1,2,\ldots,i, \tag{2.36}$$

In summay we solve the governing equations (2.28) subject to the initial condition (2.30) and the boundary conditions (2.31) and (2.35).

2.3.3 Determination of Inner Boundary Conditions

The amount, $P_k(t)$, of precipitate k is governed by

$$\frac{dP_k}{dt}=\begin{cases}S\{m_k(t)-q_k(t)\}-\lambda_k P_k+\lambda_{k-1}P_{k-1}, & 0<t<T_L,\\ -Sq_k(t)-\lambda_k P_k+\lambda_{k-1}P_{k-1}, & t>T_L,\end{cases} \quad \text{subject to } P_k(0)=0, \tag{2.37}$$

where $S=4\pi r_1^2$ [cm^2] is the surface area of the waste solid. The analytical expressions for $q_k(t)$ and $m_k(t)$ are obtained below.

The amount of the precipitate will decrease by radioactive decay and dissolution into the water phase. The dissolved radionuclide will diffuse away from the precipitate. The rate, $q_k(t)$, of removal of radionuclide k from the precipitate by molecular diffusion at $r=r_1$ is defined as

$$q_k(t)=-\varepsilon D_{e(k)}\frac{\partial N_k}{\partial r}\bigg|_{r=r_1},\ t>0. \tag{2.38}$$

The concentration gradient at r_1 is obtained by differentiating $N_k(r,t)$ with respect to r. $N_k(r,t)$ is the solution obtained by solving eq. (2.28) subject to the initial condition (2.30), the boundary condition (2.31), and the solubility-limited boundary condition,

$$N_k(r_1,t)=\gamma_k(t)\,N_{e(k)}^*,\ t>0, \tag{2.39}$$

instead of (2.35). The analytical solution has been obtained elsewhere [7], from which the diffusive mass flux, $q_k(t)$, can be derived as

$$q_k(t)=\varepsilon D_{e(k)}\varphi_k(t)\left\{\frac{1}{r_1}+\sqrt{\nabla_k}\coth\left(\sqrt{\nabla_k}L\right)\right\}$$

$$+ \frac{2\varepsilon D_{e(k)}}{L} \sum_{m=1}^{\infty} \alpha_m \left(\frac{\varphi_k(t)}{\delta_k} - \int_0^t \exp\left(-\delta_k(t-\tau)\right) \varphi_k(\tau) d\tau \right)$$

$$- \frac{2\varepsilon D_{e(k)}}{L} \sum_{j=1}^{k-1} \left[\frac{D_{e(j)}}{K_{e(k)}} \left\{ \prod_{n=j}^{k-1} \lambda_n \right\} \sum_{n=j}^{k} \frac{\sum_{m=1}^{\infty} \beta_m^2 \int_0^t \exp\left(-\delta_n(t-\tau)\right) \varphi_j(\tau) d\tau}{\prod_{\substack{n=j \\ n \neq j}}^{k} \left(\delta_n - \delta_j\right)} \right], \; t > 0, \; k = 1, 2, \ldots, i, \quad (2.40)$$

where

$$\nu_k = \frac{K_{e(k)} \lambda_k}{D_{e(k)}}, \; L = r_2 - r_1, \; \alpha_m = \beta_m^2 \frac{K_{e(k)}}{D_{e(k)}}, \; \delta_k = \lambda_k + \alpha_m, \; \beta_m = \frac{m\pi}{L}, \; \varphi_k(t) = \gamma_k(t) N_{e(k)}^*,$$

$$k = 1, 2, \ldots, i. \quad (2.41)$$

The amount of the precipitate increases due to the radioactive decay of the precursor and the release of radionuclide k by alteration of the waste solid. If we assume that the glass alters at a constant rate over the leach time T_L, the congruent release rate, $m_k(t)$, is obtained by solving:

$$\frac{dm_k}{dt} = -\lambda_k m_k + \lambda_{k-1} m_{k-1}, \; 0 < t < T_L, \; k = 1, 2, \ldots, i, \; \lambda_0 = 0, \quad (2.42)$$

subject to $m_k(0) = m_k^o$, where m_k^o [mol/m^2·yr] is defined as

$$m_k^o = \frac{M_k^o}{S T_L}, \quad (2.43)$$

and M_k^o [mol] is the inventory of radionuclide k in the waste solid at the beginning of the waste-solid alteration. (2.42) is mathematically equivalent to the Bateman equation, whose solutions are readily available [8] as

$$m_k(t) = m_k^o e^{-\lambda_k t} + \sum_{j=1}^{k-1} \left[m_j^o \left\{ \prod_{n=j}^{k-1} \lambda_n \right\} \left(\sum_{n=j}^{k} \frac{\exp\left(-\lambda_n t\right)}{\prod_{\substack{n=j \\ n \neq j}}^{k} \left(\lambda_n - \lambda_j\right)} \right) \right], \; 0 \le t \le T_L. \quad (2.44)$$

With (2.40) and (2.44), the solution to (2.37) is obtained as

$$P_k(t) = F_k(t) \exp(-\lambda_k t) + \sum_{j=1}^{k-1} \left\{ \prod_{n=j}^{k-1} \lambda_n \right\} F_j(t) \sum_{n=j}^{k} \frac{\exp(-\lambda_n t)}{\prod_{\substack{j=j \\ j \neq j}}^{k} \left(\lambda_j - \lambda_n\right)}, \; t \ge 0, \quad (2.45)$$

where $F_k(t) = g(t) * S\left[m_k(t) \left\{ h(t) - h(t - T_L) \right\} - q_k(t) \right]$. $\quad (2.46)$

To evaluate $\gamma_k(t)$ exactly based on the definition (2.34), we have to know N_k. Thus, the problems must be solved iteratively. To decouple the precipitation analysis from the radionuclide diffusion analysis for the bentonite region, we approximate the definition of $\gamma_k(t)$ as

$$\gamma_k \approx \frac{\int_0^{T_L} m_k(t)dt}{\sum_e \int_0^{T_L} m_k(t)dt}. \tag{2.47}$$

Notice that γ_k is reduced to a constant by utilizing the analytical solution for $m_k(t)$ given by (2.44). This approximation is good for long-lived radionuclides such as uranium isotopes. However, if the radionuclide has a smaller initial inventory than its precursor and the solubility is relatively large, then the precipitate will not be created until sufficient accumulation is achieved in the waste solid due to the decay of the precursor. This could occur for the case of the ^{243}Am —> ^{239}Pu —> chain.

$P_k(t)$ is initially zero by the initial condition. $P_k(t)$ increases with time at early times if more radionuclide k is released from the glass log by alteration of the glass matrix than diffuses away from the precipitate (refer to the right-hand side of eq. (2.37)). Eventually $P_k(t)$ starts to decrease because the congruent release rate decreases or even becomes zero after the leach time while the diffusive mass flux stays almost constant as long as the precipitate exists there. Finally, $P_k(t)$ becomes zero at some time t_k^*. Thus, for this case, a positive t_k^* is obtained by solving $P_k(t_k^*) = 0$, and the precipitate k exists until the time, t_k^*, and the boundary condition (2.32) applies.

If the solubility is high enough, or the half-life of the radionuclide is short enough, the right-hand side of (2.37) becomes negative right after $t = 0$, and so $P_k(t) < 0$ (no precipitation occurs) for $t > 0$. For this case, no positive t_k^* is obtained by solving $P_k(t_k^*) = 0$, and the congruent-release boundary condition (2.34) applies.

Precipitation can occur not only at the interface ($r = r_1$) but also in the bentonite region, if the precursor has a greater retardation coefficient, a greater solubility and a shorter half-life. In the present analysis, we neglect precipitation of radionuclides within the bentonite region, based on the result of the previous analysis for diffusion of a ^{241}Am —> ^{237}Np —> decay chain [9]. This analysis shows that precipitation in the bentonite region has minor effects on the mass release rate at the bentonite/rock interface, and that the effects become even smaller if the lifetime of the metal canister is longer than 6000 years.

2.3.4 Analytical Solutions

The Laplace-transformed analytical solutions for (2.28) subject to the side conditions (2.30), (2.31), and (2.32) or (2.34) are obtained as follows:

$$\tilde{N}_k(r, s) = \tilde{N}_k^{(k)}(r, s) + \sum_{j=1}^{k-1} \tilde{N}_k^{(j)}(r, s) \tag{2.48}$$

where

$$\tilde{N}_k^{(k)}(r, s) = \frac{r_1 \psi_k}{Q_{kk}} \exp(-\phi_k L) \frac{1}{r} \sinh\{\phi_k (r_2 - r)\} \tag{2.49}$$

$$\tilde{N}_k^{(j)}(r,s) = r_1 \tilde{\psi}\left[\prod_{n=}^{k-1}\left(\chi_{n+1}\nu_n\right)\right]\sum_{n=}^{k} a_n^{(j)} \exp\left(-\phi_n L\right)\frac{\sinh\left\{\phi_n\left((r_2 - r)\right)\right\}}{r\prod_{\substack{=\\ \neq n}}^{k}\left(\phi_{\ell}^2 - \phi_n^2\right)}, \tag{2.50}$$

$$Q_{kj} = \frac{1}{2}\left\{\left(H_k\phi_j + J_k\right) + \left(H_k\phi_j - J_k\right)\exp\left(-2\phi_j L\right)\right\}, \tag{2.51}$$

$$H_k = \left(1 - \sigma_k\right)\varepsilon D_{e(k)},\ J_k = \sigma_k + \frac{H_k}{r_1},\ \phi_j = \sqrt{\frac{K_{e(j)}(s+\lambda_j)}{D_{e(j)}}},\ \chi_k = \frac{D_{e(k-1)}}{D_{e(k)}}, \tag{2.52}$$

$$a_n^{(j)} = \sum_{m=}^{n-1} a_m^{(j)} \frac{Q_{nm}}{Q_{nn}} \frac{\prod_{\substack{=\\ \neq m}}^{n-1}\left(\phi_{\ell}^2 - \phi_n^2\right)}{\prod_{\substack{=\\ \neq m}}^{n-1}\left(\phi_{\ell}^2 - \phi_m^2\right)},\ a_j^{(j)} = \frac{1}{Q_{jj}},$$

$$a_n^{(j)} = 0, n \le j-1, \tag{2.53}$$

$$\nu_k = \frac{K_{e(k)}\lambda_k}{D_{e(k)}},\ \nu_0 = 0, \tag{2.54}$$

and s is a complex Laplace variable. The coefficient $a_n^{(j)}$ is defined in a recursive way. The tilde ~ symbol stands for a Laplace-transformed function. $\tilde{\psi}_k$ is the Laplace-transform of $\psi_k(t)$, which appears in the symbolically represented boundary condition (2.35) and is given in (2.36).

Either σ_k = 1 or 0 should be substituted into the above analytical solution, depending on the boundary condition, (2.32) or (2.34), which is determined by the precipitation analysis shown in Section 2.3.3.

With the analytical solution (2.48), the Laplace-transformed diffusive mass flux of radionuclide k at the EBS surface, $r = r_2$, is derived as

$$\tilde{Q}_k = -\varepsilon D_{e(k)} \frac{\partial \tilde{N}_k}{\partial r}\bigg|_{r=r_2}$$

$$= \frac{\varepsilon D_{e(k)} r_1}{r_2}\left\{\frac{\tilde{\psi}_k \phi_k}{Q_{kk}}\exp\left(-\phi_k L\right) + \sum_{j=1}^{k-1}\tilde{\psi}\left[\prod_{m=}^{k-1}\left(\chi_{m+1}\nu_m\right)\right]\sum_{m=}^{k} a_m^{(j)} \frac{\phi_m \exp\left(-\phi_m L\right)}{\prod_{\substack{=\\ \neq m}}^{k}\left(\phi_{\ell}^2 - \phi_m^2\right)}\right\}. \tag{2.55}$$

(2.55) is the source term function for the transport in the host rock, used in the boundary condition, (2.8).

2.3.5 Limitations of the Source Term Model

In summary, we made the following assumptions for the model simplification :

• The mass flux at the waste-solid surface is assumed to be expressed as a linear combination of two major contributions: dissolution of precipitates and congruent release from the waste solid.

• The isotopic fraction of the precipitate, $\gamma_k(t)$, is approximated as a constant by (2.34).

• The concentration of the radionuclide at the EBS surface is assumed to be zero.

• No matter how fractures intersect the EBS, the mass transport in the EBS is assumed to have no angular dependency.

2.4 NUMERICAL RESULTS AND DISCUSSIONS

2.4.1 Input Data

Table 2.1 Assumed parameter values

Radius of the equivalent spherical waste glass, r_1	0.337 m §
Radius of the equivalent spherical bentonite region, r_2	1.23 m §
Surface area of the waste glass, $S = 4\pi r_1^2$	1.43 m^2
Surface area of the bentonite region, $S_2 = 4\pi r_2^2$	19.1 m^2
Leach time, T_L	4×10^6 or 4×10^4 yr §
Porosity of the bentonite region, ε	0.3 §
Density of the bentonite region, ρ	2100 kg/m^3 §
Porosity of the host rock, ε_p	0.01 #
Density of the host rock, ρ_p	2600 kg/m^3 §
Porosity of the fractures, ε_f	1 *
Water velocity in fractures, v	1.0 m/yr §
Longitudinal dispersion coefficient, D^L	0
Tortuosity correction factor for the bentonite, τ	1
Tortuosity correction factor for the host rock, τ_p	0.055 §
Fracture aperture, $2b$	6.3×10^{-4} m §
Fracture spacing, $2a$	1 m #
Repository dimension, L_R	2000 m
Fracture opening area, $S_f = 2bL_R$	1.26 m^2
Number of waste canisters, n_w	40,000 #
Number of fractures intersecting the repository, n	2,000
EBS-NBS interface factor, A	3.30×10^{-3}

§: from Ref. [6] #: from Ref. [4] *: By the assumption that there is no fracture-filling material.

PWR spent fuel initially enriched at 4.5% with a burnup of 45,000 MWD/MT and a specific power of 38 MW/MTU is assumed to be stored for four years for cooling before reprocessing. At reprocessing, we assume that 99.3% of plutonium and 99.85% of uranium are recovered. We assume arbitrarily that 1% of iodine existing in the spent fuel goes into HLW, to show the radiological impact of iodine. We assume that HLW from 1 MT of PWR spent fuel is vitrified with borosilicate glass and contained in one waste canister. The vitrified HLW is assumed to be stored for fifty years before emplacement in the repository. The waste glass is assumed to start radionuclide release to the bentonite region one thousand years after the emplacement. We set the origin of the time axis ($t = 0$) at the moment when radionuclide release starts.

Parameter values for the repository configuration, the barrier properties, and the hydrologic conditions in the geologic formation are summarized in Table 2.1. The radii of the equivalent-

sphere waste package and bentonite region are calculated based on the dimensions of the cylindrical waste package and the bentonite region, which are proposed in [6] and shown in Figure 2.2.

Table 2.2 Input data for radionuclides and determined boundary conditions.

Nuclide	Half-life [yr]	Initial Inventory$ M_k^o [mol]	ALI* [Bq/yr]	t_k^* [yr]			
				T_L = 4×10^6 yr	T_L = 4×10^4 yr		
				Case (a)	Case (b)	Case (c) #	Case (d) #
				No recovery		90% recovery	99% recovery
				Fig. 2.4	Fig. 2.4 Fig. 2.5	Fig. 2.6	Fig. 2.6
Pu-240	6.57E+03	2.00E-01	2.7E+04	1.5E+05	1.8E+05	1.7E+05	1.7E+05
U-236	2.34E+07	5.59E-02	4.5E+05	1.3E+08	1.2E+08	1.2E+08	1.2E+05
Th-232	1.41E+10	5.83E-06	2.6E+04	C	1.6E+05	8.5E+04	7.8E+04
Ra-228	5.76	2.38E-15	8.6E+04	C	C	C	C
Th-228	1.91	7.00E-12	2.0E+05	C	C	C	C
Ra-224	1.00	3.68E-14	3.1E+05	C	C	C	C
Cm-245	9.30E+03	7.55E-03	2.6E+04	C	C	C	C
Am-241	4.58E+02	2.82E-01	2.7E+04	C	2.9E+03	C	C
Np-237	2.14E+06	4.02	1.8E+04	3.0E+07	3.0E+07	2.3E+07	1.6E+07
U-233	1.62E+05	1.24E-03	4.1E+05	5.2E+06	2.0E+06	2.0E+06	2.0E+06
Th-229	7.34E+03	2.57E-06	2.0E+05	C	5.9E+04	5.1E+04	4.9E+04
Ra-225	4.06E-02	1.42E-11	2.7E+05	C	C	C	C
Pu-242	3.76E+05	1.80E-02	2.9E+04	6.4E+06	7.5E+06	7.2E+06	7.1E+06
U-238	4.46E+09	5.83	5.0E+05	1.3E+09	1.2E+09	1.2E+09	1.2E+09
Th-234	6.60E-02	8.63E-11	1.1E+07	C	C	C	C
U-234	2.45E+05	1.11E-02	4.5E+05	5.6E+06	2.9E+06	2.9E+06	2.9E+06
Th-230	8.00E+04	3.11E-05	1.3E+05	9.1E+05	1.1E+05	7.5E+04	7.0E+04
Ra-226	1.60E+04	1.15E-07	7.3E+04	C	C	C	C
Am-243	7.37E+03	4.86E-01	2.7E+04	C	2.0E+04	C	C
Pu-239	2.44E+04	2.54E-01	2.7E+04	5.3E+05	5.9E+05	5.6E+05	5.6E+05
U-235	7.04E+08	7.00E-02	5.0E+05	9.0E+08	8.4E+08	8.3E+08	8.2E+08
Pa-231	3.28E+04	3.50E-07	6.9E+03	C	C	C	C
Ac-227	2.18E+01	2.32E-10	7.4E+03	C	C	C	C
Th-227	5.12E-02	5.39E-12	5.1E+06	C	C	C	C
Ra-223	3.12E-02	3.30E-13	1.7E+05	C	C	C	C
Tc-99	2.13E+05	1.03E+01	1.4E+08	1.5E+05	8.9E+05	8.9E+05	8.9E+05
I-129	1.57E+07	1.78E-02	2.0E+05	C	C	C	C
Cs-135	2.30E+06	3.48	2.6E+07	C	C	C	C

$: Inventories included in HLW generated from 1 metric ton of spent fuel. U and Pu are recovered at the reprocessing stage. Also see text in Section 2.4.1.

#: For cases (c) and (d), the specified fractions of Cm, Am, and Np are recovered from the inventory shown in the third column of the table.

*: Annual Limit on Intake [11].

Letter 'C' means that no precipitate occurs, and the congruent release boundary condition (2.8) is applied.

Two values are assumed for the leach time [6]. The longer leach time corresponds to the lower ambient temperature in the repository. The values for the porosity and the density of the bentonite are obtained from [6]. The porosity and the density of the host rock are typical for granitic rock observed in Japan [4]. Water velocity, v, in the fractures, the fracture aperture, $2b$, and the tortuosity correction factor, τ_p, of the granitic host rock are taken also from [6]. The longitudinal dispersion coefficient is assumed to be zero to obtain conservative results for the maximum concentrations in the host rock. The tortuosity correction factor, τ, for the bentonite is conservatively assumed to be unity, which overestimates the diffusion coefficients in the bentonite.

Assuming that 40,000 waste canisters to be placed in the repository with a spacing of 10 m in an array fashion, the repository has dimensions of 2,000 m × 2,000 m. With the assumed fracture spacing of 1 m [4], the number of fractures intersecting the repository is estimated as 2,000. With these numbers, the factor A can be calculated as 3.3×10^{-3} by eq. (2.12).

We consider four decay chains for actinides as shown in Table 2.2. Also considered are long-lived fission products: ^{99}Tc, ^{129}I, and ^{135}Cs. Inventories at $t = 0$ in 1 MT of spent fuel after reprocessing and the fifty-year cooling period are calculated by ORIGEN-II computer code [10]. The annual limit on intake [11] is listed for each radionuclide.

Table 2.3 summarizes the parameter values assumed for each element. Solubilities have been obtained in [6], based on the analysis by a geochemical simulation code, where granitic groundwater is assumed to react with Kunigel V1, a typical Japanese bentonite. Sorption distribution coefficients for the bentonite and for the granitic rock are also listed in [6], where the most probable values are chosen from Sorption Data Base of OECD/NEA [12]. The retardation coefficient for the fracture transport is set to be unity by assuming conservatively that no nuclides are sorbed by the fracture-filling materials. Since the tortuosity correction factor, τ, for the bentonite is assumed to be unity, the diffusion coefficients in the bentonite are assumed to be identical to those in free water.

Table 2.3 Assumed elemental parameters

Element	Solubility	In the bentonite			In the host rock			
	N_e^* [mol/m^3]	K_d^e [m^3/kg]	K_e [1]	D_e [m^2/yr]	R_e [1]	K_{dp}^e [m^3/kg]	α_e [1]	D_e^l [m^2/yr]
Cm	2.8E-04	1.0	4.9E+03	1.2E-02		5.0E-01	1.3E+03	6.6E-06
Am	5.0E-05	1.3	6.4E+03	1.2E-02		1.3	3.3E+03	6.6E-06
Pu	2.3E-11	6.6E-02	3.2E+02	1.2E-02		5.9E-02	1.5E+02	6.6E-06
Np	1.5E-09	6.7E-03	3.4E+01	1.2E-02		1.6E-02	4.1E+01	6.6E-06
U	9.6E-08	4.1E-03	2.1E+01	1.2E-02		2.0E-03	5.2	6.6E-06
Pa	2.7E-04	1.0E-01	4.9E+02	1.2E-02	1	1.0E-02	2.6E+01	6.6E-06
Th	1.8E-07	1.0E-01	4.9E+02	1.2E-02		3.7E-01	9.5E+02	6.6E-06
Ac	8.1E-01	1.0	4.9E+03	7.0E-02		2.5E-01	6.4E+02	3.9E-05
Ra	3.5E-06	9.2E-01	4.5E+03	3.3E-02		4.3E-02	1.1E+02	1.8E-05
Tc	3.9E-05	8.5E-04	5.2	1.2E-02		8.4E-05	2.3E-01	6.6E-06
I	——	1.8E-04	1.9	7.0E-02		5.3E-04	1.4	3.9E-05
Cs	——	1.1E-02	5.5E+01	7.0E-02		5.7E-03	1.5E+01	3.9E-05

2.4.2 Computer Code

A computer code (TTB) has been developed, which can calculate (a) the space-time-dependent concentration profiles of radionuclides in the bentonite region by eq. (2.48) and in the fracture by eq. (2.17), (b) the time-dependent mass fluxes of radionuclides at the bentonite surface

by eq. (2.55) and at an arbitrary downstream location in the fracture by eq. (2.27), and (c) the congruent release rates of radionuclides from the waste glass by eq. (2.44).

To compare radiological toxicity of radionuclides, we define the "hazard" as the ratio of annual radioactivity release [Bq/yr] of radionuclide k at a certain location to the annual limit on intake [Bq/yr] of radionuclide k. The TTB code can calculate the hazards of the waste solid, at the bentonite surface, and at the arbitrary location in the fracture.

First, the TTB code determines the boundary condition at the waste glass surface, by the precipitation analysis shown in Section 2.3.3. With the analytical solution, (2.45), t_k^* is obtained by solving $P(t_k^*) = 0$ numerically by the bisection method, for which the subroutine DZBREN of IMSL Library [13] has been utilized.

With the determined boundary condition, the analytical solutions are evaluated by making inverse Laplace transforms numerically, based on the Talbot method [14]. The readily available computer program [15] for this method has been utilized.

2.4.3 Inner Boundary Conditions

The radionuclide concentration history at the boundary at $r = r_1$ are shown in the right half of Table 2.2. To compare these, we consider four cases: (a) T_L = 4 million years with no recovery of radionuclides from HLW, (b)T_L = 40,000 years with no recovery, (c)T_L = 40,000 years with 90% recovery of Am, Cm, and Np, (d)T_L = 40,000 years with 99% recovery of Am, Cm, and Np. The table shows the times when precipitates disappear, t_k^*. By comparison of case (a) with case (b), we can observe the effect of the leach time. Cases (b), (c), and (d) compare the effect of actinide recovery.

We observe that, in case (b), precipitates of plutonium and americium will exist for a longer time period than in case (a). In case (a), the initial congruent release rates are hundred fold smaller than in case (b) by eq. (2.43). Since the half-lives of ^{243}Am and ^{241}Am are relatively short, compared with the leach times, less americium precipitate can accumulate at a smaller release rate from the waste solid. On the other hand, because, due to the ^{237}Np half-life (2.14 million years), ^{237}Np released from the waste solid can accumulate as precipitate with small loss by radioactive decay even for the case of T_L = 4 million yr, the lifetime of ^{237}Np precipitate is 30 million years for cases (a) and (b).

Uranium precipitates exist for a shorter time period in case (b) than in case (a). With the longer leach time of the glass (case (a)), by radioactive decay of its precursors, more uranium can be accumulated in the waste glass before it is released. This can be confirmed by Figure 2.3, which shows that hazards from uranium isotopes, which are proportional to the inventories in the waste solid, increase with time toward the end of the 4 million yr leach time.

Of the fission products considered here, only Tc has the solubility-limited boundary condition.

By recovering Cm, Am, and Np (compare cases (b), (c) and (d)) from initial HLW before vitrification, americium precipitate will never occur. The neptunium precipitate lifetime becomes shorter by recovery.

2.4.4 Radionuclide Release from the EBS

Figure 2.3 shows the potential hazards resulting from ingestion of all radionuclides contained in the fraction of the waste glass altering every year for T_L =40,000 yr and 4 million yr. This can be considered as the theoretical maximum for the hazard that could result from the burial of the waste solids. The magnitude of the total hazard is two orders of magnitude greater in the case of T_L = 40,000 yr than in the 4 million yr case by eq. (2.43). Contributions from ^{241}Am, ^{243}Am, and ^{239}Pu are dominant in the 40,000 yr case. For the 4 million yr case, ^{237}Np and its daughter ^{229}Th become significant after those radionuclides.

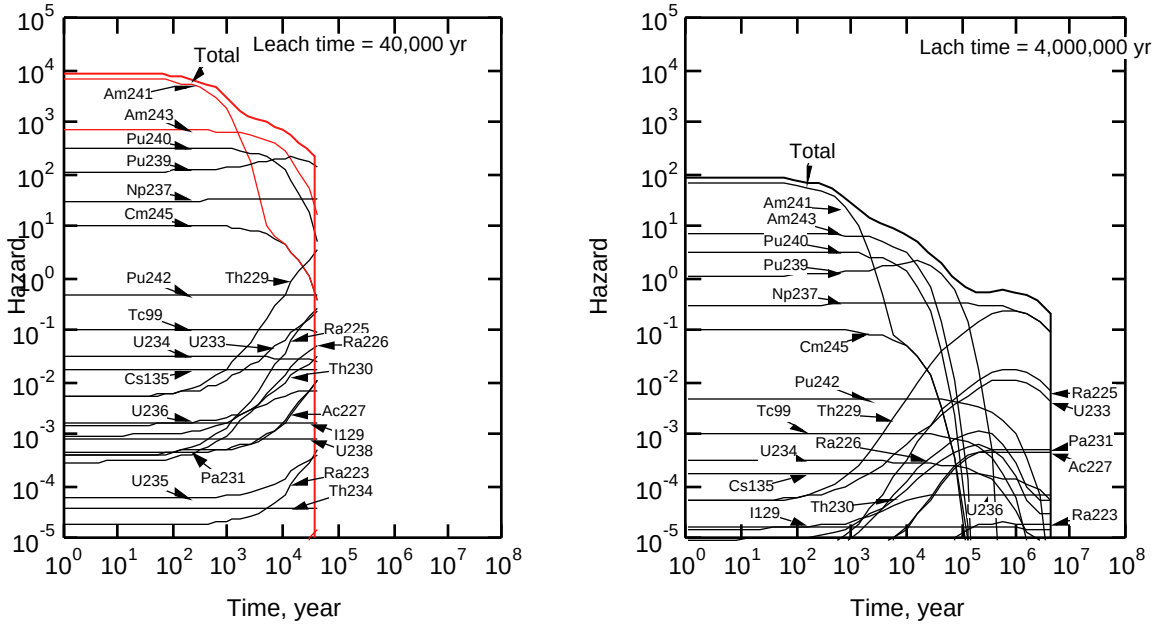

Figure 2.3 Radiological hazards resulting from ingestion of radionuclides at $r = r_1$ contained in the fraction of the waste solid that alters every year. For the left figure, the waste solid is assumed to alter for 40,000 years at a constant rate. For the right figure, 4 million year is assumed.

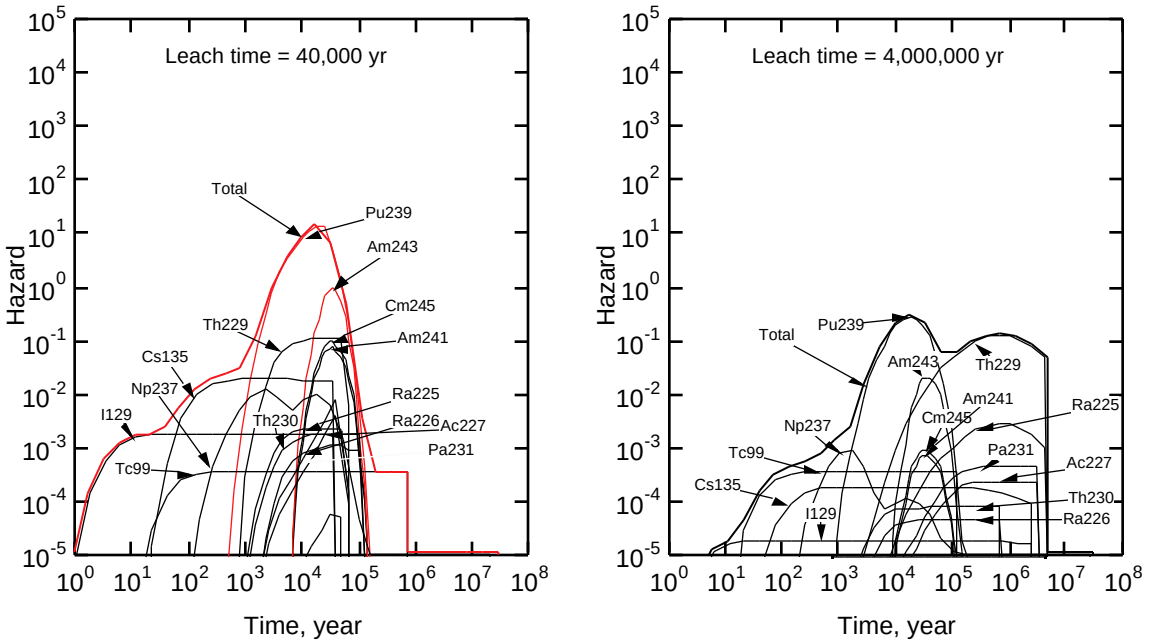

Figure 2.4 Radiological hazards of radionuclides released at the outer surface at $r = r_2$ of the bentonite region for T_L = 40,000 and 4 million years.

Figure 2.4 shows the annual hazard resulting from ingestion of radionuclides released at the outer surface of the bentonite region for the same leach times as assumed in Figure 2.3. For both cases, after diffusion in the bentonite region, the total hazard is reduced by more than two orders of magnitude (compare Figure 2.3 and Figure 2.4). ^{239}Pu dominates the total hazard there

for about one hundred thousand years. The early-time hazard results from the weakly-sorbing, long-lived fission-product nuclides. Americium isotopes, which are the major contributors to the total hazard in the waste form, become less significant at the bentonite surface, $r = r_2$, because of their relatively short half-lives, very low solubility, and strong sorption with the bentonite.

With the two orders of magnitude longer leach time, hazards of ^{135}Cs, ^{129}I, and ^{245}Cm are reduced by the same factor, because they are released from the waste solid congruently with the waste solid alteration.

The ^{239}Pu hazard is reduced approximately by a factor of hundred by the longer leach time, although Pu is solubility-limited. ^{239}Pu released at the bentonite surface consists of that originally existing in the waste solid and that created by decay of ^{243}Am while diffusing in the bentonite region. The former contribution is not influenced by the leach time because the excess amount of Pu released from the waste solid will precipitate. The latter contribution becomes smaller with the longer leach time, because Am is released congruently for the case of 4 million yr leach time.

Initially, there exist negligible amounts of daughters of ^{237}Np and uranium isotopes in the waste solid. Since ^{237}Np and uranium isotopes form precipitates that last for a longer time than the leach times, hazards of such daughter nuclides as ^{229}Th and ^{225}Ra are not affected by change in the leach time. Thus, for T_L = 4 million yr, the contribution of ^{229}Th becomes relatively prominent after the ^{239}Pu regime, among contributions from Cm, Am, Pu, and fission-product nuclides which are reduced by a factor of hundred.

2.4.5 Radionuclide Transport in the NBS

Figure 2.5 shows the hazard resulting from a single waste form at locations 10 m and 100 m away from the bentonite surface as a function of time.

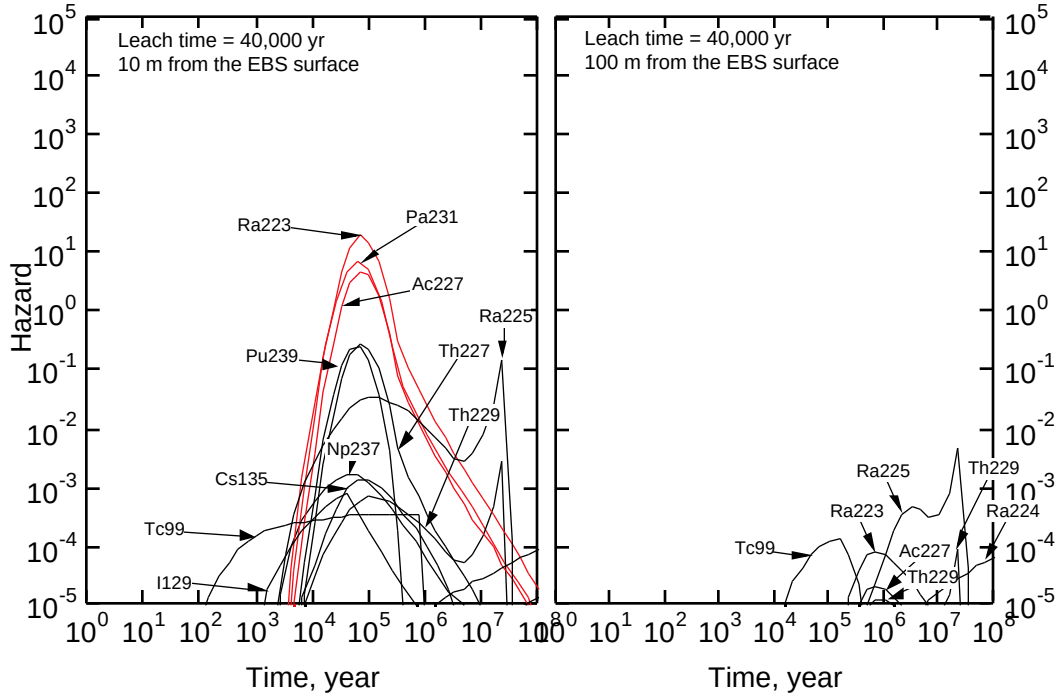

Figure 2.5 Radiological hazards of radionuclides in the natural barrier. Transport distance through the fractures is 10 m (left) or 100 m (right). The leach time is assumed to be 40,000 yr.

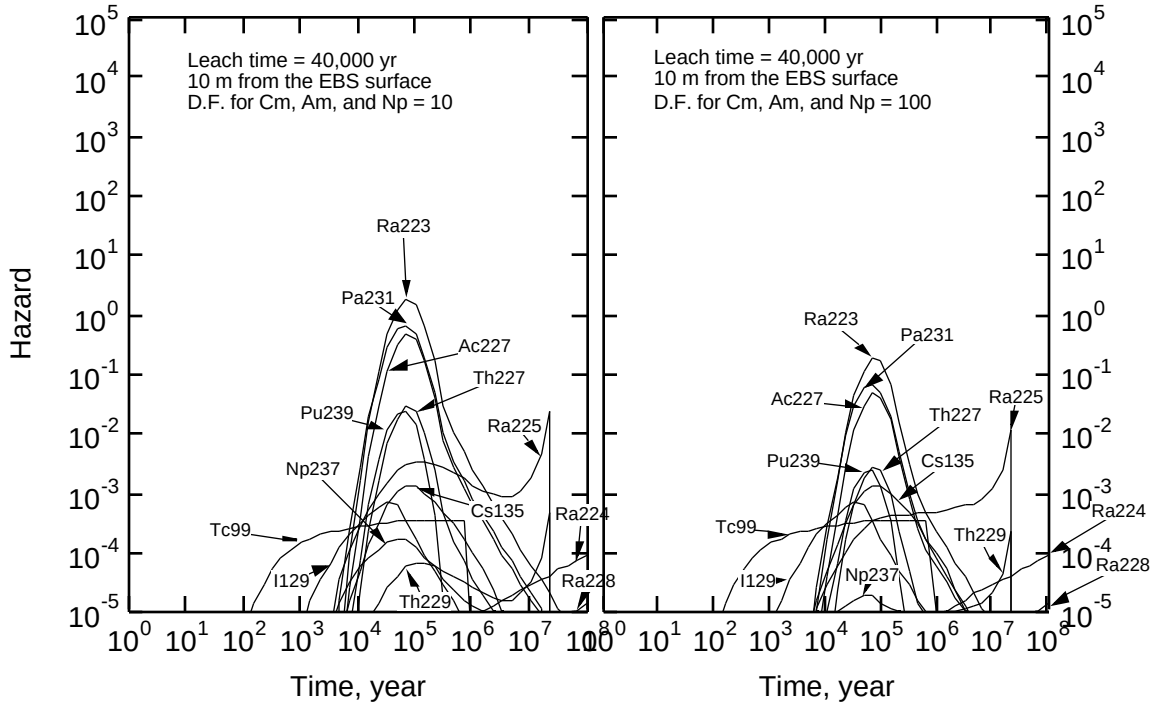

Figure 2.6 Effect of recovering Cm, Am, and Np from the waste solid. 90% (left) or 99% (right) recovery is assumed. No recovery case is shown in the left graph of Figure 2.5. The leach time is 40,000 yr. Transport distance from the engineered barrier surface is 10 m.

The major contributors at the 10 m location are ^{223}Ra, ^{231}Pa, and ^{227}Ac. The ^{239}Pu hazard, which is the most important at the bentonite surface, is now approximately 1% of the maximum total hazard. Cm, Am, and Pu decay to negligible levels, and in return, contributions from ^{231}Pa, ^{227}Ac, and ^{223}Ra, which are higher-generation members of the decay chains, become important. The early-time hazard is still dominated by ^{99}Tc.

At the 100 m location, only a few radionuclides survive. The major contributors are now ^{99}Tc, ^{223}Ra, and ^{225}Ra. The total hazard is reduced to less than 1% of the unit hazard. If the maximum total hazard is compared with that of the waste solid shown in Figure 2.3, more than six orders of magnitude reduction is achieved with the engineered barriers and the 100 m-thick natural barrier.

Considering that the repository dimensions are 2,000 × 2,000 m^2, we can point out the possibility of reducing the radiological hazard by reserving a relatively small region around the repository domain. In this region, the major contributors to the total hazard shift from Cm, Am, and Pu, which have significant initial inventories in the waste solid, to Th, Ra, Pa, and Ac, which practically do not exist in the waste solid initially. Thus, the region around the engineered barriers has a crucial role for the repository performance.

Because the region will be disturbed by construction of the repository and emplacement of heat-generating waste solids, mass transport analyses in this region will require separate geochemical and hydrological analyses.

2.4.6 Effect of Minor Actinides Recovery from HLW

Figure 2.6 shows the hazard observed at the 10 m location for the cases where 90% and 99% of ^{245}Cm, ^{243}Am, ^{241}Am, and ^{237}Np are recovered from the original HLW before

vitrification. Together with the left graph of Figure 2.5, the effects of minor actinide recovery can be observed.

Since ^{239}Pu, ^{231}Pa, ^{227}Ac, ^{227}Th, and ^{223}Ra are generated from ^{243}Am, recovery of ^{243}Am affects the hazards from those radionuclides directly. Recovery of ^{245}Cm, ^{241}Am, and ^{237}Np reduces the hazards of ^{229}Th and ^{225}Ra. Thus, because the minor actinides eventually decay to radium and thorium, which are the major contributors in the natural barrier, the total radiological hazard from the geologic disposal of HLW is reduced by recovery of minor actinides. The reduction is approximately proportional to the amount recovered. However, as shown in Figure 2.5, with a 100 m-thick region around the repository, the total radiological hazard can be reduced to a negligible level. Thus, recovering the minor actinides from HLW does not improve the radiological safety or shorten the time span for the safety assessment for the geologic disposal system, and should be considered from a different safety aspects, such as the human-intrusion scenario and the criticality-safety scenario.

2.5 CONCLUSIONS

By determining the boundary conditions for multiple-member decay chains of actinides based on the detailed analysis of precipitation at the waste-form alteration location, numerical evaluations have been made for actinide transport in a porous bentonite region of the engineered barriers and in the fractures in the surrounding host rock. The following conclusions are obtained.

In the waste form, the major hazard contributors are ^{243}Am and ^{241}Am. With the engineered barriers, the total hazard is reduced by a factor of more than 100. The major hazard contributors at the bentonite/rock interface are ^{239}Pu, ^{229}Th, and ^{243}Am. ^{129}I, ^{99}Tc, and ^{135}Cs contribute the early-time hazard, but the magnitudes are negligibly small. If the waste form alters more slowly, the total hazard at the engineered barrier/rock interface becomes smaller because the contributions from radionuclides released congruently with the waste-form alteration are reduced.

After 10 m transport through the fractures in the host rock, ^{223}Ra, ^{231}Pa, and ^{227}Ac become dominant. After 100 m transport, ^{99}Tc, ^{223}Ra, and ^{225}Ra are the major contributors. Between these two points, approximately four orders of magnitude reduction in the total hazard is achieved. Since the major contributors in the host rock are the decay daughters of minor actinides, recovery of minor actinides from HLW reduces the total hazard in the natural barrier. However, since the radiological hazard can be attenuated within the 100-m thick geologic formation around the repository, the merit for recovery of the minor actinides is questionable from the view point of radiological safety.

The region in the vicinity of the engineered barriers is very important in the context of the safety assessment because the radiological hazard reduces to a negligible level within this region. The region, however, might be disturbed by construction of the repository and emplacement of heat-generating waste forms. Further mass-transport analysis should be performed for the region in the vicinity of the repository by taking into account differing geochemical, hydrological and mechanical properties from those in the undisturbed host rock.

2.6 REFERENCES FOR CHAPTER 2

[1] D. P. Hodgekinson and P. R. Maul, 1-D Modeling of Radionuclide Migration Through Permeable and Fractured Rock for Arbitrary Length Decay Chains Using Numerical Inversion of Laplace Transforms, *Ann. Nucl. Energy*, **15**(4), 175-189 (1988).

[2] T. H. Pigford, Actinide Burning and Waste Disposal, MIT International Conference on the Next Generation of Nuclear Power Technology, UCB-NE-4176 (1990).

[3] D. H. Tang, E. A. Sudicky and E. O. Frind, Contaminant Transport in Fractured Porous Media: Analytical Solution for a Single Fracture, *Water Resources Research,* **17**, 555–564 (1981).
[4] Power Reactor and Nuclear Fuel Development Corporation, *Technical Report on Research and Development for Geological Disposal of High-Level Radioactive Wastes*, PNC TN 1410 92-08 (1992).
[5] NAGRA, Kristallin-I: Safety Assessment Report, Tech. Rep. 93-22E, Nagra, Wettingen, Switzerland (1994).
[6] J. Ahn, T. Ikeda, T. Ohe, T. Kanno, Y. Sakamoto, T. Chiba, M. Tsukamoto, S. Nakayama, S. Nagasaki, K. Banno, and T. Fujita, Quantitative Performance Allocation of Multi-Barrier System for High-Level Radioactive Waste Disposal, *Journal of Atomic Energy Society of Japan,* **37**(1), 59-77 (1995).
[7] P. L. Chambré, T. H. Pigford, W. W.-L. Lee, J. Ahn, S. Kajiwara, C. L. Kim, H. Kimura, H. Lung, W. J. Williams, and S. J. Zavoshy, Mass Transfer and Transport in a Geologic Environment, Lawrence Berkeley Lab., LBL-19430 (1985).
[8] M. Benedict, T. H. Pigford, and H. W. Levi, Nuclear Chemical Engineering, Second Ed., Chapter 2, McGraw-Hill, New York (1981).
[9] J. Ahn and A. Suzuki, Diffusion of the ^{241}Am —> ^{237}Np Decay Chain Limited by Their Elemental Solubilities in the Artificial Barriers of High-Level Radioactive Waste Repositories, *Nuclear Technology*, **101**, 79--91 (1993).
[10] A. G. Croff, *A User's Manual for the ORIGEN 2 Computer Code*, ORNL/TM-7175, Oak Ridge National Laboratory (1980).
[11] Announcement No. 15 by Science and Technology Agency, Government of Japan (1988).
[12] A. B. Muller, *NEA Compilation of Chemical Thermodynamic Data for Minerals Associated with Granite*, OECD/NEA, Paris (1985).
[13] IMSL, Math Library, FORTRAN Subroutines for mathematical Applications, IMSL Inc., Houston, Texas.
[14] A. Talbot, The Accurate Numerical Inversion of Laplace Transforms, *J. Inst. Math. Applic.*, **23**, 97-120 (1979).
[15] J. A. Barker, Laplace Transform Solutions for Solute Transport in Fissured Aquifers, *Adv. Water Resources,* **5**, 98 (1982).

CHAPTER
THREE

MASS TRANSPORT IN DISTURBED ZONE

3.1 INTRODUCTION AND BACKGROUND

Results of the previous chapter show that the engineered barriers can limit release of most radionuclides to the surrounding host rock far below their annual limits on intake, and that host rock of 100-meter thickness can furthermore achieve sufficient attenuation of radioactivity.

To be more confident with such results, radionuclide transport must be investigated in more detail in the host rock region adjacent to the engineered barrier system (EBS). Geochemical, hydrological, and rock-mechanical properties should be different from those of undisturbed host rock.

At the emplacement of the waste form, bentonite is dry and compacted initially. Excavation of main repository tunnels and deposition holes introduces fractures in the vicinity of the EBS in addition to originally existing fractures. Some fractures intersecting the EBS connect with a fracture network bearing groundwater flow, while others do not (see Figure 3.1).

Through fractures connecting with a water-bearing fracture network, water is supplied to initially dry bentonite. Water is imbibed mainly by capillary suction, and the bentonite swells (see Chapter 4). Excess bentonite then extrudes into the fractures intersecting the EBS.

Imbibition from the tip of the extruding bentonite becomes weaker as bentonite swells, and eventually all of the bentonite gets wet. By the time bentonite becomes completely wet, dead-end fractures, i.e., fracture segments that do not connect to the water-flowing fracture network but intersect the EBS, will also be filled with swollen bentonite.

It is observed that bentonite extrudes to a greater distance in fractures of larger aperture [1]. Fractures of large aperture are more likely to connect the EBS with the water-flowing fracture network because they tend to have greater areal extension. Radionuclides that are released from the EBS and survive the transport through the fractures filled with extruding bentonite will be released to the water-flowing fracture network. In this chapter, we focus on the effect of the bentonite intrusion into intersecting fractures from the standpoint of radionuclide confinement.

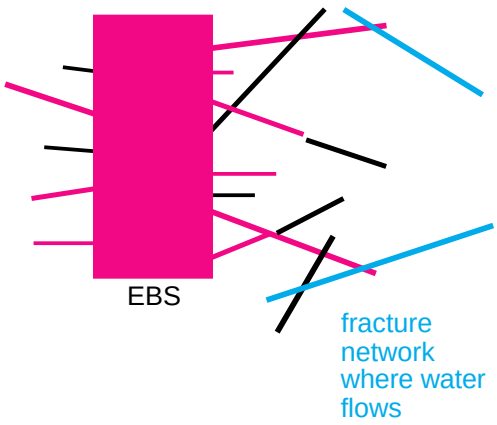

Figure 3.1 Conceptual transport path around EBS. Bentonite extrudes into intersecting fractures, part of which are linked with the water-flowing fractures.

3.2 MATHEMATICAL MODEL

3.2.1 Governing Equations

We consider the configuration depicted in Figure 3.2. To simplify the mathematical analysis, a planar geometry is adopted, based on the previous study by Kang [2]. We assume that radionuclides are released from the waste form located at the center of the EBS. Bentonite surrounds the waste form. Planar, parallel fractures of aperture $2\grave{b}$ intersects the bentonite with spacing $2\grave{d}$ at a right angle. The parallel fractures represent the fractures connecting with the water-flowing backbone fracture network. All minor dead-end fractures distributed in between two adjacent fractures are homogenized with matrix pores. The porosity of the region between two adjacent fractures is ε_p, which includes both the rock matrix pores and the dead-end minor fractures. Due to disturbance introduced during the repository construction, the porosity ε_p is assumed to be greater than the porosity of undisturbed rock matrix. The parallel fractures is filled with the extruding bentonite up to the distance $\grave{L}$ from the fracture mouth.

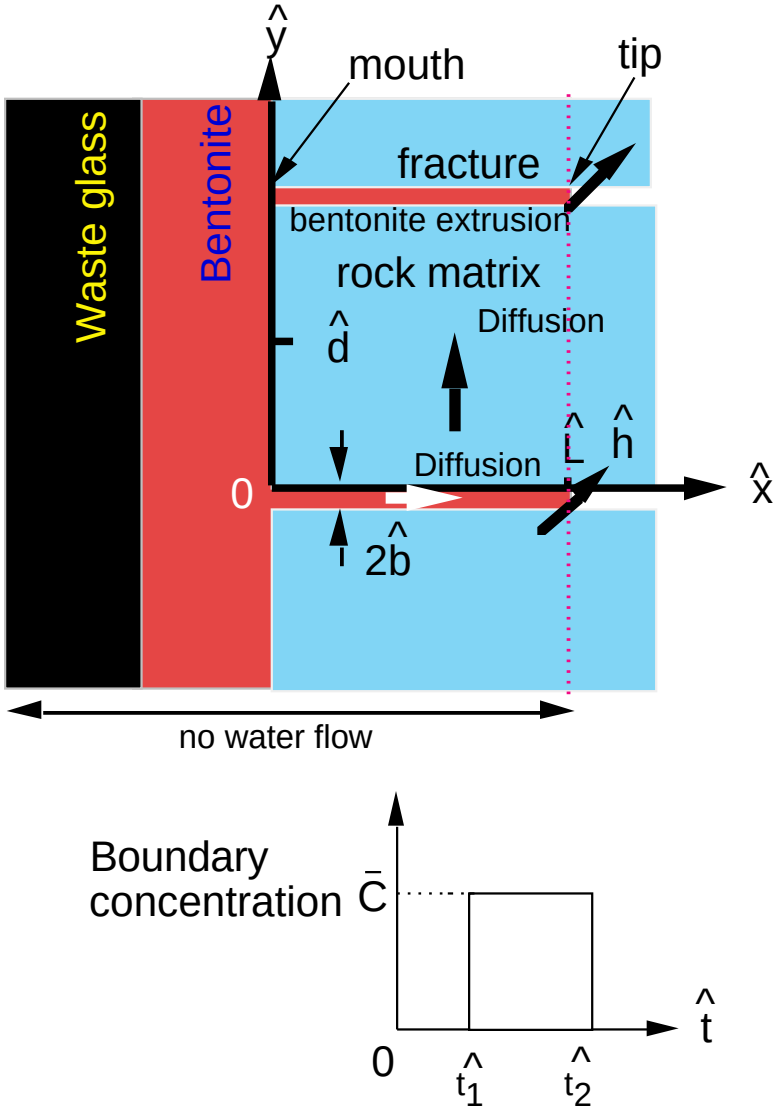

Figure 3.2 The engineered barrier intersected by planar fractures.

$\dot{L}$ is assumed to be constant with time. This assumption is introduced primarily for simplification, and must be revisited after we obtain quantitative knowledge about the transient swelling behaviour of bentonite (the effort for this is initiated in Chapter 4.). In reference [1], it is observed that bentonite swelling is initially rapid and reaches a steady state. Thus, assuming that $\dot{L}$ is constant is equivalent to the assumption that, by the time radionuclides begin to enter the extruding bentonite from the mouth, bentonite swelling reaches a steady state.

Radionuclides released from the waste form diffuse in the bentonite in the EBS. Because the rock matrix has smaller porosity and tortuosity than the extruding bentonite, diffusion in the rock matrix is likely to be slower than in the extruding bentonite in the fractures. Therefore, radionuclides in bentonite in the EBS will diffuse toward the fracture mouth, which acts like a funnel, and then diffuse in the extruding bentonite. Matrix diffusion from the fractures into the rock matrix is also considered. At the tip of the extruding bentonite, radionuclides are released to the water flowing in the fractures. Only molecular diffusion is considered in the region between the center of the EBS and the tips of the extruding bentonite. We neglect the effect of precursors in radioactive dacay chains.

The boundary condition at the fracture mouth is simplified as the constant concentration for a time period between $\dot{t}_1$ and $\dot{t}_2$ (see Figure 3.2). Time $\dot{t}_1$ represents the delay due to diffusion in the EBS, and $\dot{t}_2 - \dot{t}_1$ the time period of radionuclide release from the EBS.

At the tip of the extruding bentonite, radionuclides are released to the water flowing in the direction perpendicular to the extruding bentonite region. At the tip, we assume that the diffusive flux from the bentonite side is equal to the mass transfer rate to the flowing water. The mass transfer coefficient at the tip is $\dot{h}$.

Then, the governing equations for the mass transport in the extruding bentonite and in the rock matrix are written as:

$$\frac{\partial C}{\partial t} = \frac{\partial^2 C}{\partial x^2} - \Lambda C - \frac{q}{b},\ 0 < x < 1,\ t > 0 \tag{3.1a}$$

$$\frac{\partial C_p}{\partial t} = \Delta \frac{\partial^2 C_p}{\partial y^2} - \Lambda C_p,\ 0 < x < 1,\ 0 < y < 1,\ t > 0 \tag{3.1b}$$

subject to the side conditions:

$$C(x, 0) = 0,\ 0 < x < 1 \tag{3.2a}$$

$$C_p(x, y, 0) = 0,\ 0 < x < 1,\ 0 < y < 1 \tag{3.2b}$$

$$C(0, t) = C_{av}(t),\ t > 0 \tag{3.2c}$$

$$-\frac{\partial C}{\partial x}\bigg|_{x=1} = ShC(1, t),\ t > 0 \tag{3.2d}$$

$$C_p(x, 0, t) = C(x, t),\ 0 < x < 1,\ t > 0 \tag{3.2e}$$

$$\frac{\partial C_p}{\partial y}\bigg|_{y=1} = 0,\ 0 < x < 1,\ t > 0 \tag{3.2f}$$

where $$q = -\varepsilon_p \frac{\partial C_p}{\partial y}\bigg|_{y=0}, \quad 0 < x < 1, \quad t > 0 \tag{3.3}$$

$$x = \frac{\hat{x}}{\hat{L}}, \quad y = \frac{\hat{y}}{\hat{d}}, \quad t = \frac{\hat{D}\hat{t}}{\hat{L}^2 R}, \quad C = \frac{\hat{C}}{\hat{C}}, \quad C_p = \frac{\hat{C}_p}{\hat{C}} \text{ and} \tag{3.4a}$$

$$\Lambda = \frac{\hat{\lambda}\hat{L}^2 R}{\hat{D}}, \quad \Delta = \frac{\hat{D}_p R \hat{L}^2}{\hat{D} R_p \hat{d}^2}, \quad b = \frac{\hat{D}\hat{b}\hat{d}}{\hat{D}_p \hat{L}^2}, \quad Sh = \frac{\hat{h}\hat{L}}{\varepsilon \hat{D}}, \quad t_1 = \frac{\hat{D}\hat{t}_1}{\hat{L}^2 R}, \quad t_2 = \frac{\hat{D}\hat{t}_2}{\hat{L}^2 R} \tag{3.4b}$$

$\hat{C}$ is the concentration of the radionuclide in the water phase of the extruding bentonite. C is the concentration in the water phase in the rock matrix. $\bar{C}$ is the boundary concentration at $x = 0$ in the time interval $\hat{t}_2 - \hat{t}_1$. $C_{av}(t)$ is the normalized concentration at the mouth (see Figure 3.2). $\hat{D}$ and D_p are the diffusion coefficients of the radionuclide in the extruding bentonite and in the rock matrix, respectively. R and R_p are the sorption retardation coefficients in the extruding bentonite and in the rock matrix, respectively. $\hat{h}$ is the mass transfer coefficient at the tip of the extruding bentonite. $\hat{\lambda}$ is the decay constant of the radionuclide. ε is the porosity of the extruding bentonite. Λ and Sh are Thiele and Sherwood numbers, respectively. The nondimensionalized time t is called Fourier number.

Δ is the normalized diffusion coefficient in the rock matrix. $\Delta > 1$ can be interpreted in two ways; the diffusion coefficient in the rock matrix is greater than in the extruding bentonite, or the fracture spacing are relatively small compared with the extension of the extruding bentonite, $\hat{L}$. In either case, the radionuclide concentration in the water phase in the rock matrix between two adjacent fractures becomes almost uniform. In the case of $\Delta < 1$, penetration by matrix diffusion in the rock matrix is limited in the vicinity of the fracture walls.

3.2.2 Analytical Solutions

The Laplace-transformed solution for the problem defined by (3.1a) to (3.4b) is obtained as

$$\tilde{C}(x, p) = \tilde{C}_{av}(p) \frac{F(x, p)}{F(0, p)}, \tag{3.5}$$

$$\tilde{C}_p(y, x, p) = \frac{\cosh\left[\mu(1 - y)\right]}{\cosh \mu} \tilde{C}(x, p), \tag{3.6}$$

where

$$F(x, p) = \exp\left[\varphi(x - 1)\right] - \gamma \exp\left[-\varphi(x - 1)\right], \tag{3.7}$$

$$\tilde{C}_{av}(p) = \frac{1}{p}\left[\exp\left(-t_1 p\right) - \exp\left(-t_2 p\right)\right], \tag{3.8}$$

$$\varphi = \sqrt{p + \Lambda + \frac{\varepsilon_p \mu}{b} \tanh \mu}, \quad \mu = \sqrt{\frac{p + \Lambda}{\Delta}}, \text{ and } \gamma = \frac{Sh + \varphi}{Sh - \varphi}. \tag{3.9}$$

p is a complex-valued Laplace variable. ~ denotes a Laplace transform. Inversion of Laplace transform was carried out numerically by Talbot method [3].

The mass flux at the tip of the bentonite is expressed as

$$\hat{h}\hat{C}(\hat{L}, \hat{t}) = \frac{\varepsilon \hat{D}\bar{C}}{\hat{L}} Sh \quad C(1, t). \tag{3.10}$$

We call *Sh C(1, t)* as the normalized mass flux at the tip, which can be evaluated by (3.5).

The mass flux at the mouse of the bentonite is expressed as

$$-\varepsilon \hat{D} \frac{\partial \hat{C}}{\partial \hat{x}}\bigg|_{\hat{x}=0} = -\frac{\varepsilon \hat{D}\bar{C}}{\hat{L}} \frac{\partial C}{\partial x}\bigg|_{x=0}. \tag{3.11}$$

In order to express the barrier effect of the extruding bentonite, the reduction factor, K, is defined as the ratio of the total amount of radionuclides released at the tip to the total amount entering through the mouth. By (3.10) and (3.11), the factor K is expressed as

$$K = -Sh \frac{\int_0^\infty C(1, t)dt}{\int_0^\infty \frac{\partial C}{\partial x}\bigg|_{x=0} dt}. \tag{3.12}$$

The numerator can be evaluated by numerically inverting the Laplace transform,

$$\frac{\tilde{C}(1, p)}{p} = \frac{\tilde{C}_{av}(p)}{p} \frac{F(1, p)}{F(0, p)}, \tag{3.13}$$

and the denominator

$$-\frac{1}{p} \frac{d\tilde{C}}{dx}\bigg|_{x=0} = \frac{\varphi \tilde{C}_{av}(p)}{p} \frac{\exp(-\varphi) + \gamma \exp(\varphi)}{F(0, p)}. \tag{3.14}$$

3.3 NUMERICAL RESULTS AND DISCUSSIONS

3.3.1Input Data

Table 3.1 shows typical parameter values used in the calculations.

Values for porosity (0.01) and density (2.6 g/cm^3) of the undisturbed host rock are typical for granitic rock, and the same as those listed in Table 2.1. For the bentonite in the fracture, the porosity is 0.3, and the density is 1.8 g/cm^3 [1], which is smaller than that of the compacted bentonite originally in the EBS.

In the porous matrix region between two adjacent fractures, minor fractures filled with bentonite and original host rock are homogenized. Therefore, the properties of the porous matrix should be interpolated from those of pure bentonite and undisturbed host rock.

Here, we assume arbitrarily that the porous matrix consists of 90% host rock and 10% bentonite. From the bentonite contribution, 0.1 × 0.7 = 0.07 of total volume is occupied by the bentonite solid phase, and 0.1 × 0.3 = 0.03 by the pore water phase. From the undisturbed rock contribution, 0.9 × 0.99 = 0.891 is occupied by the rock solid phase, and 0.9 × 0.01 = 0.009 by the pore water. In summary, the porosity, ε_p of the porous matrix between the fractures is 0.039, the rock fraction, s_r, is 0.891, and the bentonite fraction, s_b, is 0.07. These values are used in (3.15).

Diffusion coefficients are determined by first considering that the diffusion coefficient in free water is approximately 10^{-5} cm^2/sec, and then by multiplying tortuosity factors, 0.1 and 0.001 for the extruding bentonite and for the undisturbed host rock, respectively. If we assume that the tortuosity of the homogeneous mixture of host rock and bentonite is interpolated from the values of the pure materials based on those fractions, the tortuosity of the mixture is calculated as 0.011. Thus, we assign 10^{-6} cm^2/sec for the bentonite in the fracture, $\dot{D}$, and 10^{-7} cm^2/sec for the porous matrix, D_r. Values for the fracture spacing, the fracture aperture, and the bentonite extrusion distance are referred from [1].

With these typical values, the non-dimensionalized aperture, *b*, can be calculated as 0.015. Because it is likely that the spacing d between fracture segments connecting the EBS and the water-flowing fracture network is proportional to the bentonite extrusion distance $\dot{L}$ and the fracture aperture b, in many cases, the variation of the non-dimensionalized aperture, *b*, would be small.

Table 3.1 Parameter values applied in the calculations

Parameter	Nomenclature	Value
Porosity of extruding bentonite	ε	0.3
Porosity of rock matrix	ε_p	0.039
Diffusion coefficient in extruding bentonite	$\dot{D}$	10^{-6} cm^2/sec
Diffusion coefficient in rock matrix	D_r	10^{-7} cm^2/sec
Half spacing between two fractures	$\dot{d}$	30 cm
Bentonite extrusion distance	$\dot{L}$	10 cm
Half aperture of fracture	$\dot{b}$	0.1 mm
Density of extruding bentonite	$\dot{\rho}$	1.8 g/cm^3
Density of rock matrix	$\dot{\rho}_r$	2.6 g/cm^3
Normalized aperture	b	0.015
Sherwood number	Sh	0.03 ~ 1

The Sherwood number was estimated by the previous analysis [2], where the relation between the Peclet number and the Sherwood number was obtained (see Figure 3.3) for a different geometry. With typical repository conditions (Peclet number ranging from 1 to 100), the Sherwood number ranges between 0.03 and 1. The effect of differing geometries would be small for the numerical results obtained later, for the following reasons. For a small Peclet number region, such as Peclet number less than 1, molecular diffusion is dominant to advection. So, the effect of geometry on the relation between the Sherwood number and the Peclet number given in Figure 3.3 would be small. As Peclet number increases, the relation will deviate from the curve shown in Figure 3.3. If the Sherwood numbers are actually smaller than that shown in the figure, then the Sherwood number range assumed here (0.03 to 1) includes the actual range. If Sherwood numbers are actually greater, then we might need to include Sherwood numbers greater than 1 in the range. However, as we observe later in Figure 3.7, the effect of Sherwood number becomes insignificant for the Sherwood number greater than 10. Thus, with the range for the Sherwood number between 0.03 and 1, we can cover the most sensitive region.

Table 3.2 summarizes radionuclide data. From the results of Chapter 2, of primary concern in the EBS and its vicinity are americium, neptunium and plutonium, for which we make calculations herein.

Sorption distribution coefficients, *Kd*, for americium and neptunium in the extruding bentonite are obtained by the experiment [4], described later in Appendix for this chapter. The experimental result is summarized in Figure 3.4. *Kd* for americium is insensitive to the redox

potential, whereas that for neptunium shows about three orders of magnitude difference between the reducing condition and the oxidizing condition. Thus, in Table 3.2, values for neptunium are listed for both conditions. *Kd* for plutonium in the extruding bentonite has not been measured. We use *Kd* for Pu with compacted bentonite in Table 2.3.

The values of sorption distribution coefficients, Kd_p, for the undisturbed host rock in Table 2.3, are listed in Table 3.2 again. The value for Np is likely to be measured in the oxidizing condition for the host rock. Therefore, for Kd_p for Np in the reducing condition, the thousand fold greater value is used.

The retardation factor R_p in the porous matrix between two fractures is calculated by considering two solid phases as

$$R_p = 1 + \frac{s_r \rho_r Kd_p + s_b \rho_b Kd}{\varepsilon_p} . \qquad (3.15)$$

Notice that the normalized diffusion coefficient, Δ, is approximately 10^{-3} for radionuclides of interest here, which implies that radionuclide penetration distance into the rock is limited to the vicinity of the fracture/porous matrix interface.

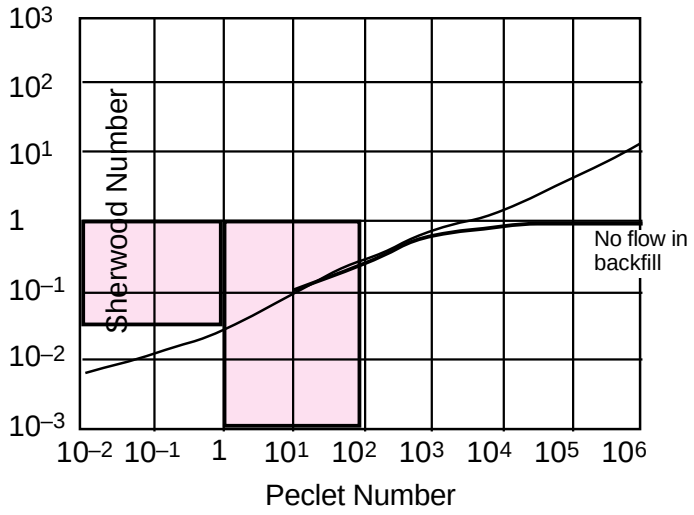

Figure 3.3 Sherwood number as a function of Peclet number [2].

Table 3.2 Parameter values assigned for each radionuclide

	Half life (sec)	*Kd* (ml/g)	Kd_p (ml/g)#	*R* ‡	R_p	Thiele moduli, Λ	Δ
^{243}Am	2.33 E11	6.5 E3	1.3E3	2.7 E4	9.8 E4	8.1	3.1 E-3
^{241}Am	1.37 E10					1.4 E2	
^{237}Np (red)	6.75 E13	6.0 E4	1.6E4##	2.5 E5	1.1 E6	2.6 E-1	2.5 E-3
^{237}Np (oxy)		3.0 E1	1.6E1	1.3 E2	1.0 E3	1.3 E–4	1.4 E-3
^{242}Pu	1.22 E13	6.6 E1	5.9E1	2.8 E2	3.7 E3	1.6 E–3	8.4 E-4
^{240}Pu	2.06 E11					9.3 E-2	
^{239}Pu	7.60 E11					2.5 E-2	

‡ $R = 1 + Kd\,\rho\,(1-\varepsilon)/\varepsilon$
# From Table 2.3.
thousand fold greater than the value listed in Table 2.3.

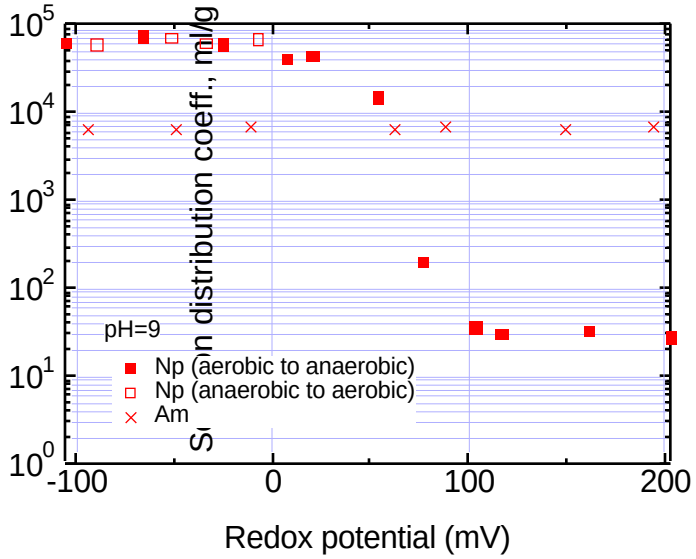

Figure 3.4 Experimental results for sorption distribution coefficients (*Kd*) of americium and neptunium with loosely compacted bentonite [4].

3.3.2Numerical Results

Figure 3.5 shows the normalized mass flux at the fracture tip as a function of Fourier number. At the fracture mouth, radionuclide supply continues for the Fourier number ranging between 10^{-2} to 10^{3}. Six curves are drawn for different Thiele moduli. These characterize different radioactive decay rates ($\Lambda = \lambda L^{2} R/D$). In each curve, one can observe that the mass flux at the tip starts to increase at Fourier number of 0.4. For Thiele numbers smaller than 10^{-1}, the trailing tail can be observed; radionuclides that have once diffused into the rock matrix come back to the fracture after the inlet boundary concentration vanishes at Fourier number of 10^{3}. For short-lived radionuclides, matrix diffusion is negligible, and so no trailing tail is observed.

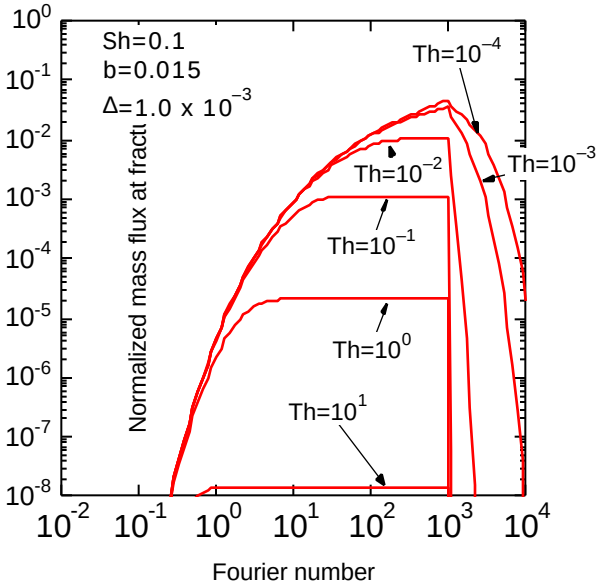

Figure 3.5 Normalized mass flux at the tip of the extruding bentonite in the fracture, as a function of Fourier number.

Penetration into rock matrix ($0 < y < 0.1$) by diffusion is depicted in Figure 3.6. Americium-243 (Thiele modulus = 8.12) decays fast, compared with the diffusion through the fracture and into the rock matrix. Penetration thickness by matrix diffusion is less than one-hundredth of the fracture spacing. Neptunium-237 can penetrate, on the other hand, up to one-tenth of the fracture spacing.

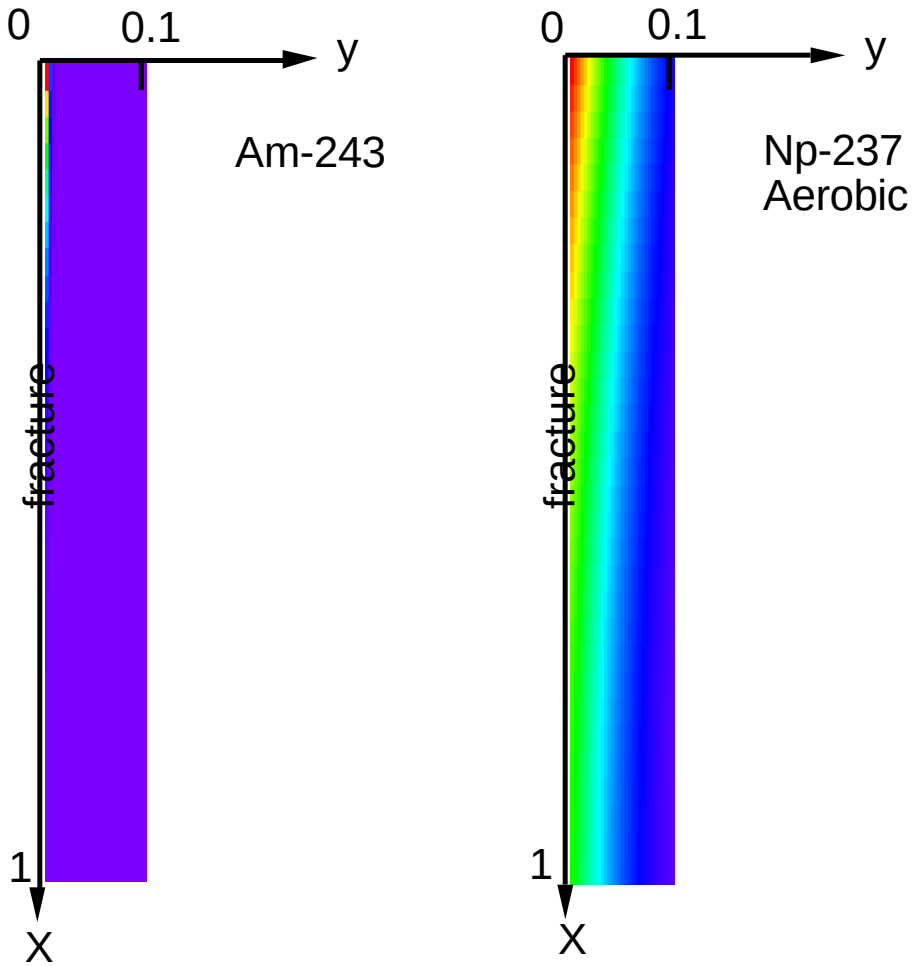

Figure 3.6 Concentration isopleths for ^{243}Am and ^{237}Np for the oxidizing condition.

In Figure 3.7, the reduction factor, (3.12), is plotted as a function of Thiele modulus, for five different Sherwood numbers, $Sh = hL/\varepsilon D$, which characferizes the effect of mass transport coefficient, $\dot{h}$. The unit reduction factor means no decay loss during the transport in the disturbed region; all that enters at the fracture mouth exits at the fracture tip. For Thiele modulus less than 10^{-6}, the reduction factor is unity for the Sherwood numbers assumed here. With Thiele moduli greater than 10, no radionuclide will be released into the water-flowing fracture network from the disturbed zone, regardless of the Sherwood number, which is determined by the water flow velocity in the fracture network. For Thiele moduli between 10^{-6} and 10, the effect of Sherwood number is important. Notice that the Thiele moduli of the radionuclides listed in Table 3.2 fall in this range. For the same Thiele modulus, a greater Sherwood number gives a less reduction factor.

This is because, with faster mass transfer at the fracture tip, radionuclide concentration becomes smaller at the tip, resulting in a greater concentration gradient in the fracture, i.e., a greater mass flux through the fracture.

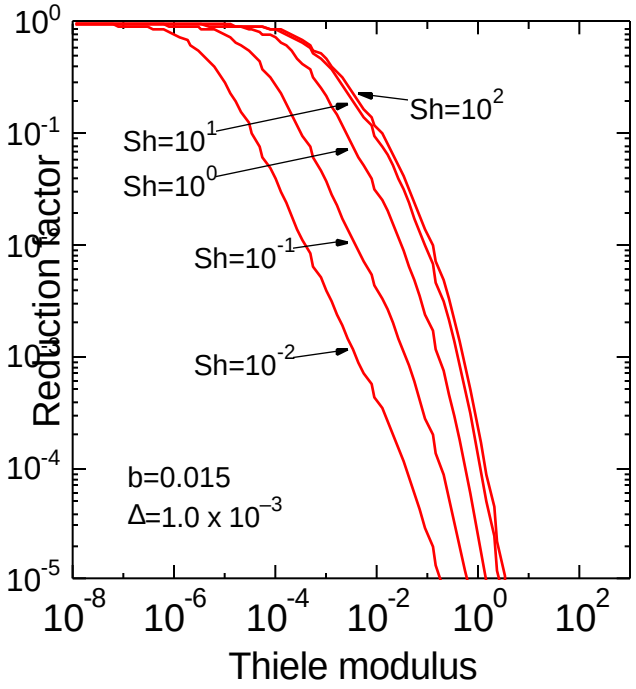

Figure 3.7 Reduction Factor vs. Thiele Modulus

Figure 3.8 shows the relationship between the reduction factor and Sherwood number for radionuclides of interest. As the mass transfer at the fracture tip increases, so does the Sherwood number, and more radionuclides are released to the outer region. Hence, the reduction factor increases. For a smaller Thiele modulus (long-lived nuclides), the reduction factor becomes greater, because more radionuclides can survive and are released at the tip. The reduction factor becomes nearly constant for the Sherwood numbers approximately greater than 10. This implies that the mass transport process in the fracture becomes the rate-limiting process.

For americium, the reduction factors are very small for the entire Sherwood number range. With the disturbed region, americium completely decays out.

In the present model, the effect of radioactive decay chain is not included. Americium-243, and -241 decay to ^{239}Pu and ^{237}Np, respectively. The results of the previous chapter for diffusion of americium and plutonium in the EBS show that amount of americium reaching the fracture mouth is already more than two orders of magnitude less than that of plutonium. Most americium in the waste glass log decays to plutonium or neptunium before it reaches the disturbed region. So, the effect of the decay of ^{243}Am to ^{239}Pu in the disturbed region on the ^{239}Pu reduction factor would be negligibly small.

The ^{237}Np inventory in the waste glass is about 20 times greater than that of ^{241}Am. The half-life of ^{241}Am is much shorter than that of ^{237}Np. Therefore, by the time both radionuclides reach the fracture mouth, most ^{241}Am has already decayed to ^{237}Np. Thus, the decay of ^{241}Am in the fracture would not increase the reduction factor of ^{237}Np.

For ^{239}Pu, ^{240}Pu, and ^{242}Pu, the reduction factors range between 10^{-4} and 10^{-2}, 10^{-5} and 10^{-3}, and 10^{-3} and 10^{-1}, respectively, for the Sherwood numbers ranging between 10^{-2} to 1.

For ^{237}Np, two cases are plotted: oxidizing and reducing. If the environment is reducing, the reduction factor is in the order of 10^{-2}. Only one percent of ^{237}Np entering the fracture can exit at the fracture tip. If oxidizing, the reduction by the disturbed region is small.

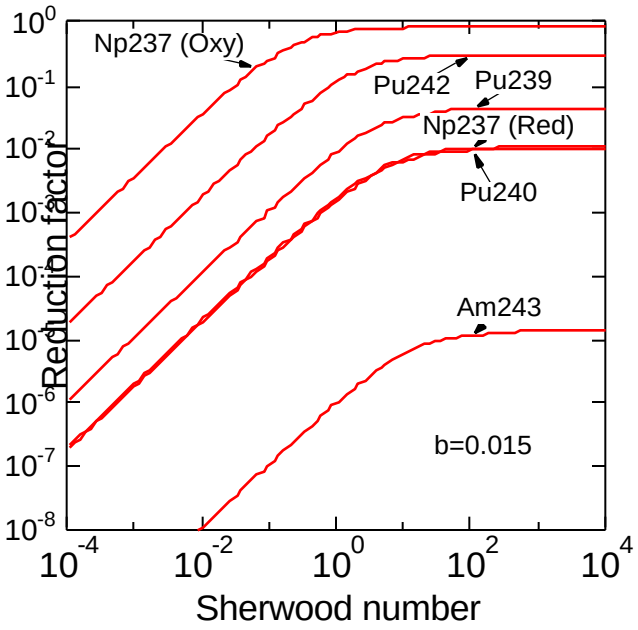

Figure 3.8 Reduction factor as a function of Sherwood number. The curve for ^{241}Am is to small to show.

3.4 CONCLUDING REMARKS

Release of radionuclides to the flowing water is reduced by radioactive decay while diffusion in the fracture is retarded by sorption and matrix diffusion. For long-lived radionuclides, matrix diffusion is the principal mechanism for retardation.

The disturbed zone can be defined as the region between the surface of the EBS and the envelope surface of the tips of the extruding bentonite in fractures.

Americium, plutonium, and, if the environment is reducing, neptunium decays to negligible levels, after transport through the disturbed zone. Thus, uranium isotopes and their daughters are released from the surface of the disturbed region, due to their extremely long half-lives.

Generally, if the Thiele modulus is greater than 10, no radionuclide will be released at the tip of the extruding bentonite with any Sherwood number. If the Thiele modulus is less than 10^{-6}, no reduction can be expected by the disturbed region.

Within the range for the Thiele modulus between 10^{-6} and 10, the effect of the mass transfer rate at the tip is important. For the mass transfer at the tip with the Sherwood number greater than 10, mass transport in the extruding bentonite becomes the rate-limiting process, and no significant effect is observed on the reduction factor.

In Chapter 2, we pointed out that the relatively short transport distance (10 ~ 100 m) in the host rock surrounding the EBS can reduce the radiological toxicity to negligible levels. With the analysis shown in Chapter 3, it has been shown that, with the disturbed region around the EBS with thickness of around 1 m, the radiological toxicity could be reduced to negligible levels. It has also been shown that the principal radionuclides released from the EBS to the outer region are uranium isotopes and their daughter nuclides. Thus, in the EBS and the disturbed region the

transport of Cm, Am, Np, and Pu is the major concern for the safety assessment, whereas in the far-field uranium family is the major concern. This observation would simplify the safety assessment of the geologic repository and reduce the uncertainty in the safety assessment.

3.5 REFERENCES FOR CHAPTER 3

[1] R. Pusch, Stability of bentonite gels in crystalline rock — Physical aspects, KBS 83-04 (1983).

[2] C.-H. Kang, Mass Transfer and Transport of Radionuclides through Backfill in a Geologic Nuclear Waste Repository, Ph. D. Dissertation, Univ. of Calif., Berkeley (1989).

[3] A. Talbot, The Accurate Numerical Inversion of Laplace Transforms, *J. Inst. Math. Applic.*, **23**, 97-120 (1979).

[4] S. Nagasaki, J. Ahn, S. Tanaka and A. Suzuki, Sorption Behavior of Np(IV), Np(V) and Am(III) in the Disturbed Zone between Engineered and Natural Barriers, submitted to*J. Radionalalytical and Nuclear Chemistry, Letter*.

3.A SORPTION RATIO MEASUREMENT

3.A.1 Materials

Americium-241 in 0.5 M HNO_3 was supplied from Amersham (Am source solution). By repeatedly mixing the Am solution with CMPO (*n*-octyl(phenyl)-N, N-diisobutylcarbamoyl-methylphosphine oxide), we prepared an Am stock solution of 1×10^{-8} M. This procedure allows removal of daughter nuclides such as ^{237}Np.

Neptunium-237 source solution in 1 M HNO_3 was obtained from CEA. To prepare a Np(IV) solution, the Np source solution was evaporated and the Np residue was dissolved in 1 M HCl. This procedure was repeated three times to ensure absence of HNO_3. The Np(V) ion in 1 M HCl was reduced by heating and adding $NH_2NH_2 \cdot HCl$. The oxidation state of Np was spectroscopically confirmed to be tetravalent. The concentration of the Np(IV) stock solution was 1×10^{-5} M. The Np(V) solution was prepared by repeatedly mixing the Np source solution with CMPO to remove impurities such as Np(IV), Np(VI), and ^{233}Pa.

Kunigel V1, Na-bentonite produced by Kunimine Industries Co. Ltd, was used in the present study . All other chemicals were analytical grade (Wako Pure Chemical Industries Co. Ltd.). Water was doubly distilled and ultrafiltered by use of 2 nm ultrafilters (Molecut UFP1, Millipore) immediately before use.

A sorption cell was prepared by sandwiching loosely compacted bentonite (0.8 g/cm^3) with two cylindrical samples of granite (20 mm in diameter and 20 mm in height). Thickness of the bentonite layer is 0.3 mm.

3.A.2 Procedure

A small amount of Am stock or Np stock was injected to the bentonite, immediately after ultrafiltering the stock solution (2 nm). pH was adjusted to 9 by addition of CO_2-free NaOH and HCl. The concentrations of Am and Np were 1×10^{-9} M and 1×10^{-8} M, respectively. These concentrations were below the solubilities of Am and Np(IV) [1,2] and were free from any error in determining sorption ratios due to precipitation.

In one series of measurements in which Am or Np(V) stock was used, Eh was changed from aerobic (+200 mV) to anaerobic (- 100 mV) conditions by addition of hydrazine. In the other series, where Np(IV) stock solution was used, Eh was changed from anaerobic (-100 mV) to aerobic (0 mV). The pH and the Eh were measured with a combination glass electrode (type

ROSS, Orion Co.) calibrated against a pH buffer solution and with a platinum electrode (type 97-78, Orion Co.).

After sorption equilibrium (one week for Am and two weeks for Np) is reached, the bentonite specimens were centrifuged and pH was checked. An aliquot was taken from the supernatant and ultrafiltered by use of a 2 nm ultrafilter. Activities of Am and Np in the ultrafiltrates were measured by a gas flow counter and a well-type Ge counter. From the initial activity of the spiked solution and the activity measured after equilibrium, sorption distribution coefficients, K_d, of Am and Np were calculated. Sorption of Am and Np on the tube walls were also investigated according to the experimental procedure of [3], and were taken into account for calculating the sorption distribution coefficients.

Experiments were carried out in inert gas boxes filled with nitrogen. The temperature was 25 ± 0.5 °C. All samples were stored in a dark place.

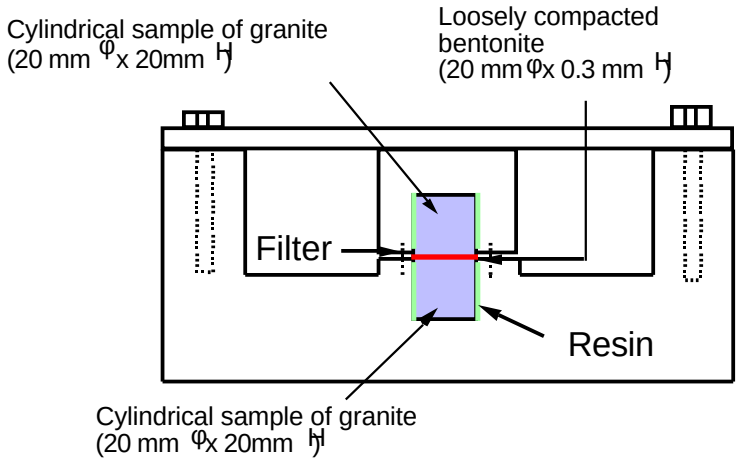

Figure 3.A.1 Sorption cell configuration

3.A.3 Results

The results are summarized in Figure 3.4 as a function of the redox potential. The sorption distribution coefficient of Am on Kunigel V1 is approximately 6.5×10^3 ml/g, which is within the range of those in the Sorption DataBase (SDB) of OECD/NEA [4].

In the anaerobic condition (between -100 mV to 0 mV) the sorption distribution coefficient of Np on Kunigel V1 is approximately 6×10^4 ml/g, which agrees with the one obtained by [5].

3.A.4 References for Appendix

[1] A. R. Felmy, D. Rai, and R. W. Fulton, *Radiochim. Acta* **50,** 193 (1990).
[2] M. I. Pratopo, H. Moriyama, and K. Higashi, *Radiochim. Acta* **51**, 27 (1990).
[3] K. H. Lieser, and R. Hill, *Radiochim. Acta* **56**, 141 (1992).
[4] K. V. Ticknor, and B. Ruegger, A Guide to the NEA's Sorption Data Base, Version 2.0 , OECD/NEA (1989).
[5] M. I. Pratopo, *et al.*, *J. Nucl. Technol.* **30**, 560 (1993).

CHAPTER
FOUR

BENTONITE RE-DISTRIBUTION IN DISTURBED ZONE

In Chapter 2, we pointed out that the relatively short transport distance (10 ~ 100 m) in the host rock surrounding the EBS can reduce the radiological toxicity to negligible levels. The transport distance has been further narrowed down to around 1 m in Chapter 3. Thus, many important phenomena affecting the repository performance occur in the vicinity of the EBS. In Chapter 3, we temporarily assumed that the bentonite extrusion distance is constant with time.

In other words, the long-term repository performance is heavily dependent on the stability of the EBS and the bentonite extruding into the disturbed rock around the EBS. The key to their stability is the long-term behaviour of the bentonite, which exists originally in the EBS.

In this chapter, therefore, we establish the mathematical model describing the bentonite swelling in the parallel fracture.

We first describe the mechanism of swelling in a microscopic level, where stresses acting on bentonite particles are characterized. We apply herein the effective stress concept. The effective stress can be interpreted as the stress acting on the skeleton of the solid phase, and is equal to the total stress minus the pore pressure. In the case of bentonite, it can be shown that the effective stress is equal to the swelling pressure, which has been measured experimentally for many clay minerals.

Based on the microscopic view of stresses, we establish a mathematical model for swelling of bentonite in a macroscopic level. We follow consolidation theory in soil science. The process of swelling is governed by the equilibrium equation for stresses acting on an element of bentonite, stress-strain relations for the solid skeleton, and a continuity equation for the pore water.

4.1 DESCRIPTION OF SWELLING IN A MICROSCOPIC LEVEL

4.1.1Basic Structural Unit

Figure 4.1 shows basic units of silica and gibbsite, which are two principal units consisting montmorillonite, the major mineral in bentonite. The silicon-oxygen tetrahedron consists of four oxygens nestled around a silicon atom to form the unit. Combining the silicon-oxygen tetrahedrons gives the silica sheet shown in the left figure. The atoms are drawn to scale on the basis of the radii in units of angstroms given in the table. The number at the right of each unit gives the valence. Combining the aluminum-oxygen octahedrons gives gibbsite. From the

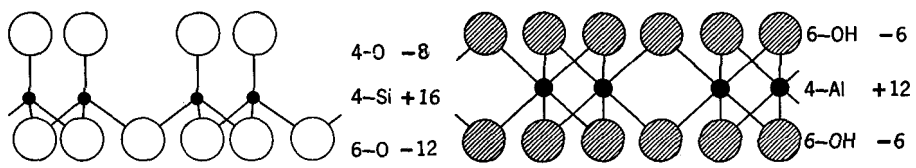

Ion	Radius (Å)	Symbol
Al^{+3}	0.57	
Si^{+4}	0.39	
O^{-2}	1.32	
OH^{-1}	1.32	
Mg^{+2}	0.78	

Figure 4.1 Basic units of silica (left) and gibbsite (right) [1].

valences shown in the figure, silica is not neutral, whereas gibbsite is. Figure 4.2 shows the dimensions of the tetrahedra and octahedra sheets.

Because both sheets have the same lattice constants (5.2 and 9.0 Å), oxygens or hydrogen peroxides on both sides of gibbsite can be shared by apical oxygens of silica. Figure 4.3 shows the mineral pyrophyllite made of a gibbsite sandwiched between two silica sheets. Montmorillonite has a structure similar to pyrophyllite with the exception that there has been isomorphous substitution of one magnesium atom for every six aluminum atoms in the gibbsite sheet.

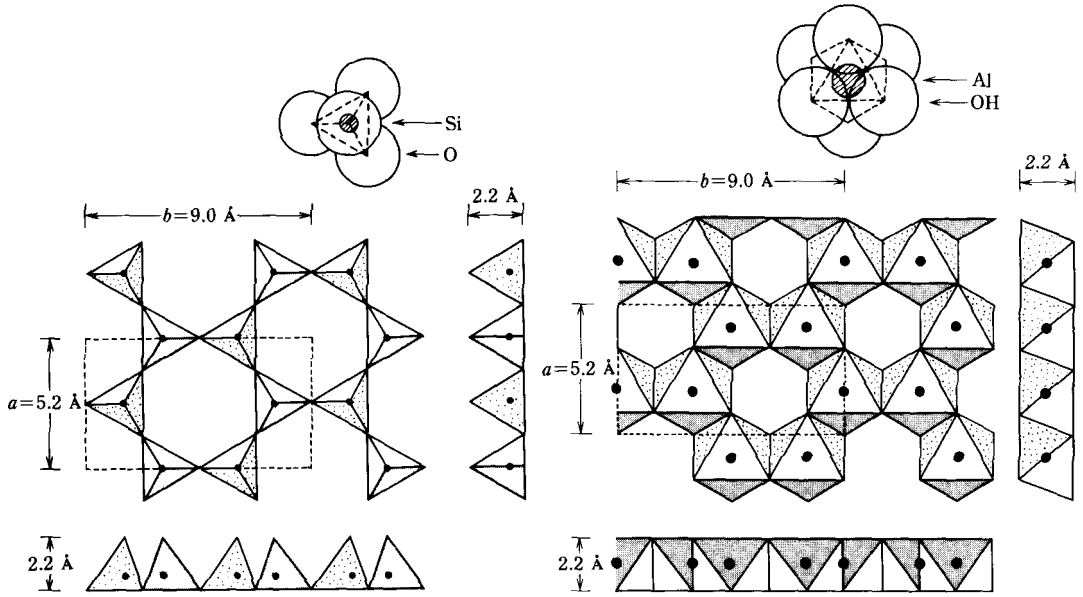

Figure 4.2 Two-dimensional views of silica and gibbsite.

4.1.2The Electrical Charge on a Bentonite Particle

With the dimensions shown in Figures 4.2 and 4.3, the specific surface and the surface area per unit charge deficiency of montmorillonite can be calculated as follows.

- The surface area per unit is: 2 (top and bottom) × 5.2 Å × 9.0Å = 93.6 $Å^2$
- Volume per unit is: 93.6 $Å^2$ ÷ 2 × 9.3 Å = 435 $Å^3$
- Weight per unit is: 435 $Å^3$ × 10^{-24} $cm^3/Å^3$ × 2.76 g/cm^3 = 1200 × 10^{-24} g
- Specific surface is: (93.6 $Å^2$ × 10^{-20} $m^2/Å^2$) ÷ (1200 × 10^{-24} g) = <u>780 m^2/g</u>

- Charge deficiency is: 1 per 6 cations in gibbsite
- 4 cations in the unit
- Charge deficiency per unit is: 2/3
- Surface area per unit charge deficiency is 93.6 $Å^2$ ÷ (2/3) = <u>140 $Å^2$</u>.

The computed values are close to the experimental values of 800 m^2/g and 133 $Å^2$ [1], respectively. Because of this large specific surface (compare 10 to 20 m^2/g for kaolinite), influence of electrical forces, which are directly related to the surface area, on the behaviour of the particle is of primary importance, and thus the particle is characterized as colloid.

4.1.3The Electrical Double Layer: General Observation

Let us now consider the nature of a particle in water. A typical particle of montmorillonite, which is one of the smallest minerals in clay, has dimensions of 1000Å × 1000 Å (surface area) ×

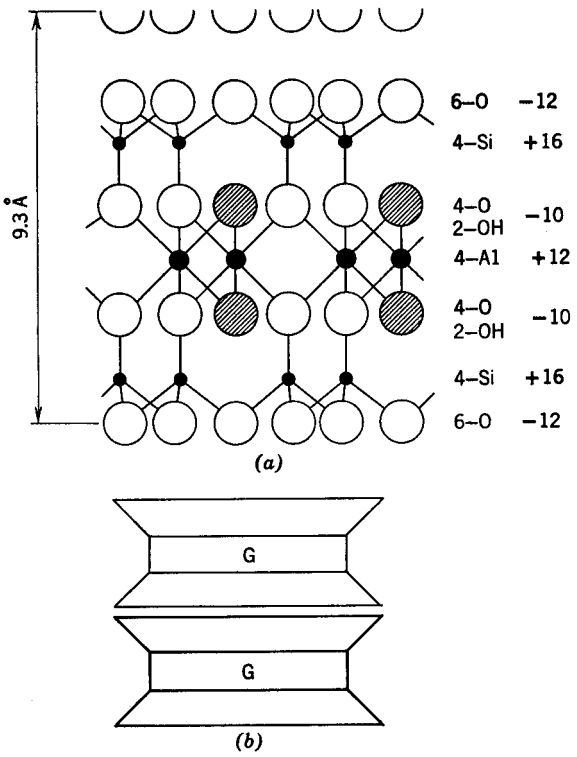

Figure 4.3 The structure of pyrophyllite. (a) Atomic structure. (b) Symbolic structure.

10Å (thickness) [1]. Considering both top and bottom surfaces, the particle has 2×10^6 Å^2 of surface area. The total number of charge deficiency on the montmorillonite particle is calculated as 2×10^6 Å^2 / 140 Å^2 = 14,000. Thus the montmorillonite particle would carry 14,000 sodium ions to compensate the charge deficiency on the particle.

If the individual particles are now dropped into water, both the mineral surface and the exchangeable ions (sodium) pick up water, i.e., hydrate. Upon hydration, the sodium ion grows about sevenfold, as illustrated in Figure 4.4. As the scaled drawings indicate, the hydrated sodium ions are too large to fit into a monoionic layer on the particles. Actually, the exchangeable ions with their shells of water move away from the mineral surfaces to positions of equilibrium. The ions are attracted to the mineral surface to satisfy the negative charge existing within the surface. They also desire to move away from each other because of their thermal energies. The actual positions they occupy are compromises between these two types of forces.

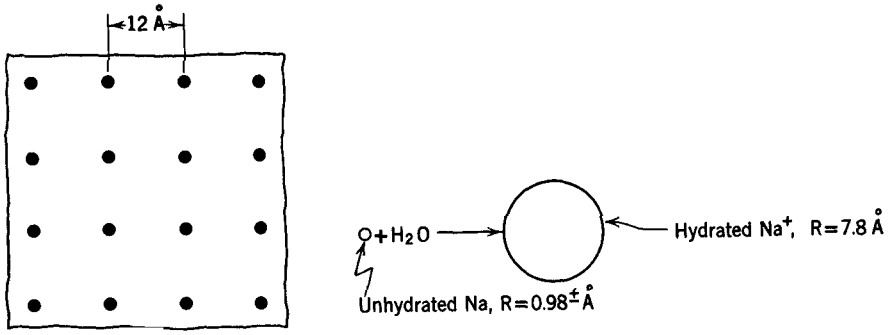

Figure 4.4 Particle surface with exchangeable ions. Surface of dry montmorillonite

Figure 4.5 shows the distributions of ions around the surface and a plot of electrical potential versus distance from the surface. The water in the double layer is under an attractive force to the particle since this water is attracted to the exchangeable ions which are in turn attracted to the soil surface (β-planes). Water is also attracted to the mineral surface by other forces such as the force between the polar water and the electrical charges on the particle surface, hydrogen bonding, and van der Waals forces. The structured region of the double layer is commonly considered to include α-planes and β-planes; the thickness of this ordered region is believed to extend to about 5Å (about two water molecules thick). If we assume that the thickness of the strongly-attracted water region is 5Å, 780 $m^2/g \times 1\ g \times 5\ Å \times 10^6\ g/m^3 = 0.4$ g of water is bound to 1 g of the solid phase.

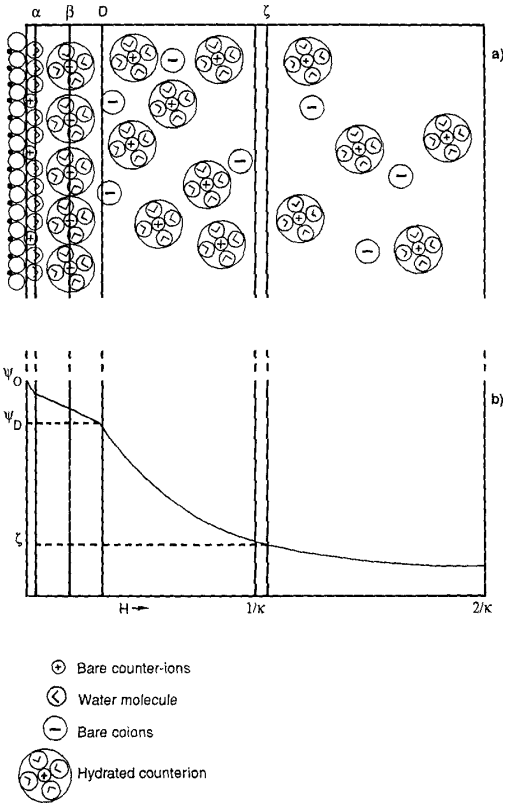

Figure 4.5 (a) A hypothetical model for a multilayer configuration of clay-water interphase. (b) Decay of the surface potential in the interphase region (clay surface is represented by the basal oxygens and the tetrahedral cations.) [2].

The α-plane (or inner Helmholtz plane) is comprised mainly of oriented water dipoles on the particle surfaces. The β-plane represents the first plane of hydrated counterions next to the surface. The D-plane (or outer-Helmholtz plane) marks the beginning of the diffuse double layer. The (1/κ) plane is most likely somewhere in the diffuse layer where the potential drops to 1/e of the surface potential. The ζ-plane is the slip (shear) plane delineating the section of the double layer that moves with the particle. This plane may be close to the (1/κ) plane. Distribution of counterions in α-planes and β-planes is expected to be discrete in the form of an array. Potential is assumed to drop linearly from the particle surface to α- and β-planes and then decay exponentially within the diffuse layer.

If we take two particles in water which are far apart and then bring them toward each other, they will reach an interparticle spacing at which they begin to exert forces on each other. Since each particle carries a net negative charge, the two particles repel each other because of the Coulombic electrical force between like charges. We denote this force as *R'*. Since the negative charge on a particle is balanced by the cations in the double layer, the two advancing particles begin to repel each other when their double layers come into contact with one another. The repulsive force between the adjacent particles for any given spacing is therefore directly related to the sizes of the double layers on the two particles.

In addition to a repulsive force between the approaching particles, there is also a component of attractive force *A'* between two particles. This attractive force is the van der Waals' force, acting between all adjacent pieces of matter.

Net energy of interaction can be estimated, based on the preceding argument [3]. The plot of the net energy versus the interparticle distance may take many forms depending on the double layer parameters, such as the distance parameter κ, the surface potential Ψ_0, the cation concentration, and so on. The main features of the net potential curve is schematically illustrated in Figure 4.6.

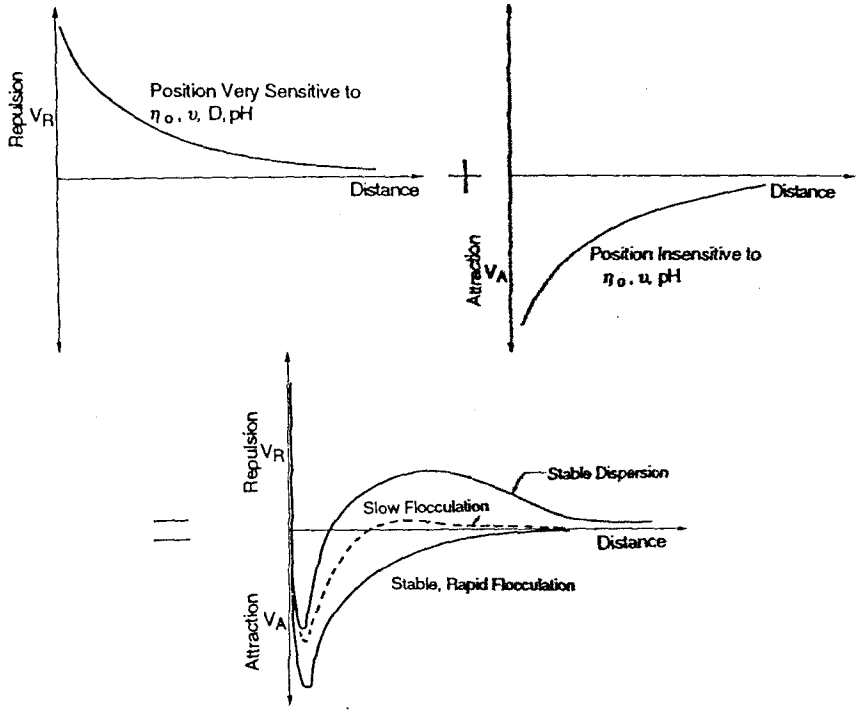

Figure 4.6 Energies of repulsion, attraction, and net curves of interaction for parallel plates.

Although the model based on the double layer theory is successful in explaining many important features of clay minerals, serious shortcomings are also reported. Low [2] reviewed his experimental data collected during the last thirty years on the swelling of a large number of Na-montmorillonite, and found a great discrepancy between the measured swelling pressure and the pressure calculated based on the view described above. He claimed that about 2% of counterions dissociate into the diffuse layer; the rest remaining in the Stern layer. Low proposed in his hydration theory an empirically derived equation expressing the relationship between the swelling pressure π (in atmospheres) and the water/clay mass ratio w in the system

$$\pi + 1 = B \exp\left(\frac{\alpha}{w}\right) \tag{4.1}$$

where B and α are empirical constants to be determined by experiments.

Although the hydration theory can reproduce experimental measurements very well, it lacks mechanistic basis. Two empirical constants represent all the complexity.

In summary, a theory that consistently explains observations with various clay minerals has not yet been developed.

4.1.4 Effective Stress

In a highly schematic way, the types of forces that exist between two adjacent particles are (see Figure 4.7):

F_m: the force where the contact is mineral-mineral,
F_a: the force where contact is air-mineral or air-air,
F_w: the force where the contact is water-mineral or water-water,
R': the electrical repulsion between particles, and
A': the electrical attraction between the particles.

The forces acting across the surface must be equal to the stress multiplied by the area:

$$\sigma\, dd = F_m + F_a + F_w + R' - A' \tag{4.2}$$

where σ is the total stress, or

$$\sigma = \sigma_m a_m + p_a a_a + p_w a_w + R - A \tag{4.3}$$

where

$$R = \frac{R'}{dd},\quad A = \frac{A'}{dd} \tag{4.4}$$

and a_m, a_a, a_w are the fractions of the surface occupied by the mineral, air, and water, respectively. p_a and p_w are the air and water pressures, respectively.

The contact stress σ_m in montmorillonite can be zero, due to its structure. In saturated medium, a_a and p_a are zero. In a partially saturated medium, $a_m \approx 0$, and $a_a + a_w \approx 1$. Thus, (4.3) is written as

$$\sigma = p_a(1 - a_w) + p_w a_w + R - A. \tag{4.5}$$

With Bishop's parameter χ [4], which is to be determined by experiments and has a strong non-linear relation to saturation S, i.e., $\chi = \chi(S)$, $0 \le \chi \le 1$, (4.5) can be written as

$$\sigma = p_w \chi + R - A. \tag{4.6}$$

χ becomes unity when the medium is saturated with water ($S = 1$).

The last two terms, $R - A$, represent the swelling pressure π. Thus,

$$\sigma = p_w \chi + \pi \tag{4.7}$$

Now we define the effective stress σ' as

$$\sigma' = \sigma - p_w \chi \tag{4.8}$$

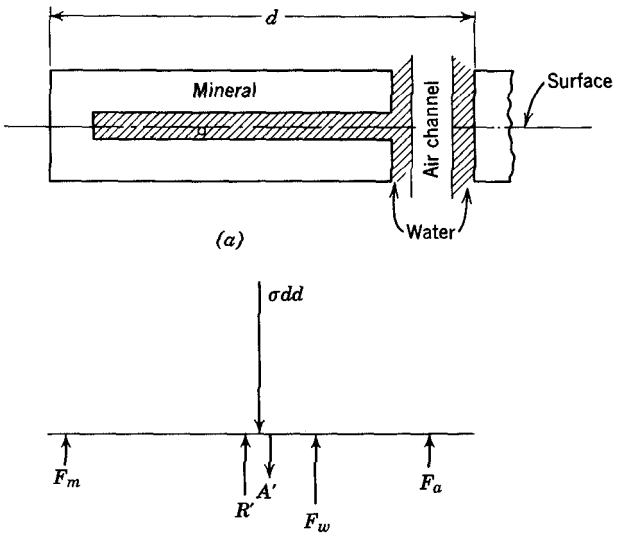

Figure 4.7 Forces between particles.

The total stress σ acts over the entire area under consideration (including solid skeleton and voids), and the pore water pressure acts over the total area minus the mineral contact area. The effective stress is approximately the force carried by the skeleton divided by the total area of the surface. Comparing (4.7) with (4.8), we obtain

$$\sigma' = \pi \tag{4.9}$$

We now make an assumption that is reasonable under most field conditions that the total stress σ at any point in the system does not change in time. Then, the changes in effective stress (or the swelling pressure by (4.9)) and pore water pressure are related by

$$\Delta\sigma' = -\left(\chi\Delta p + p\Delta\chi\right), \tag{4.10}$$

or

$$\frac{d\sigma'}{dp} = -\chi', \text{ where } \chi' = \chi + p\frac{d\chi}{dp} \tag{4.11}$$

4.2 MATHEMATICAL MODEL FOR SWELLING

4.2.1 Governing Equations

The fundamental equation of transient groundwater motion is a mass conservation equation. For a flow region which deforms with time, it can be expressed in an integral form as

$$-\int_\Gamma \rho_w \vec{q}\cdot\vec{n}\,d\Gamma = \frac{D}{Dt}\int_V \rho_w\theta\,dV, \tag{4.12}$$

where ρ_w is the water density, θ the volumetric moisture content, $\vec{q}$ is the vector flux density of water relative to the solid particles and *D/Dt* denotes the material derivative. If the volume element is appropriately small so that ρ_w and θ can be treated as average values over *V*, then (4.12) becomes

$$-\int_{\Gamma} \rho_w \vec{q} \cdot \vec{n} d\Gamma = \frac{D}{Dt}(\rho_w \theta V). \tag{4.13}$$

We now introduce Darcy's law for the equation of motion in the form

$$\vec{q} = -\frac{k\rho_w g}{\mu} \nabla h, \tag{4.14}$$

where k , g, and μ are absolute permeability, gravitational constant, and viscosity coefficient of water, respectively. h is the total head, and is broken into two components:

$$h = h_e + \frac{p_w}{\gamma_w}, \tag{4.15}$$

where h_e is the elevation head, and γ_w the specific weight of water.

If we assume that the elevation is fixed during the time interval, $Dh_e/Dt = 0$, and that ρ_w, V, and θ are functions of only p_w, substitution of (4.14) into (4.13) leads to

$$\int_{\Gamma} \rho_w \frac{k\rho_w g}{\mu} \nabla h \cdot \vec{n} d\Gamma = M_c \frac{Dp_w}{Dt}, \tag{4.16}$$

where

$$M_c = \frac{d}{dp_w}(\rho_w n S V), \tag{4.17}$$

$$\theta = nS, \tag{4.18}$$

and n is the porosity. M_c represents the mass of fluid which the volume element V can absorb due to a unit change in the average value of p_w over V. If we assume that water is incompressible, (4.17) can be calculated as

$$M_c = \rho_w S V_s \frac{de}{dp_w} + \rho_w e V_s \frac{dS}{dp_w}, \tag{4.19}$$

where we note that $nV = V_v = eV_s$, where V_s is the volume of the solid phase, constant over time and V_v is the void volume. In the light of (4.11), the first term of the right hand side of (4.19) becomes

$$\frac{d(nV)}{dp_w} = -V_s \chi' \frac{de}{d\sigma'}. \tag{4.20}$$

With (4.9),

$$\frac{d(nV)}{dp_w} = -V_s \chi' \frac{de}{d\pi}. \tag{4.21}$$

According to the Terzaghi's one-dimensional consolidation theory [5], e is a function of effective stress σ' and σ' in turn is a function of the total head h. In soil mechanics literature, it is customary to express stress-strain relationships by plotting e versus σ' or π. Figure 4.8 shows an example of the relation. Analysis of a large number of uniaxial test data indicates that a plot of e versus log σ' is approximately a straight line. The slope of the best-fitting straight line is called the 'swelling index' C_s, obtained as

$$C_s = -\frac{de}{d\log_{10}\sigma'} = 2.303\sigma' a_v, \tag{4.22}$$

where $a_v = -\frac{de}{d\sigma'}$, the coefficient of compressibility. (4.23)

With (4.20) and (4.23), the first term of (4.19) can be written as

$$\rho_w S \frac{d(nV)}{d\ p} = \rho_w S V_s a_v \chi'. \quad (4.24)$$

Substituting (4.24) into (4.19) gives the final expression for M_C as

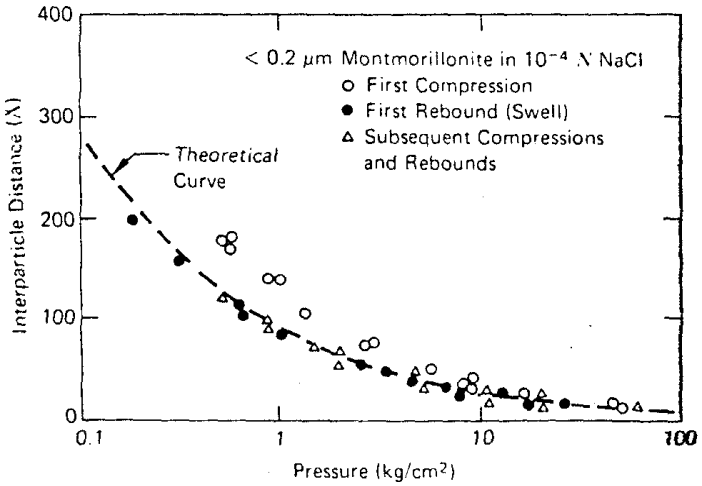

Figure 4.8 Variation of void ratio in relation to swelling pressure [3].

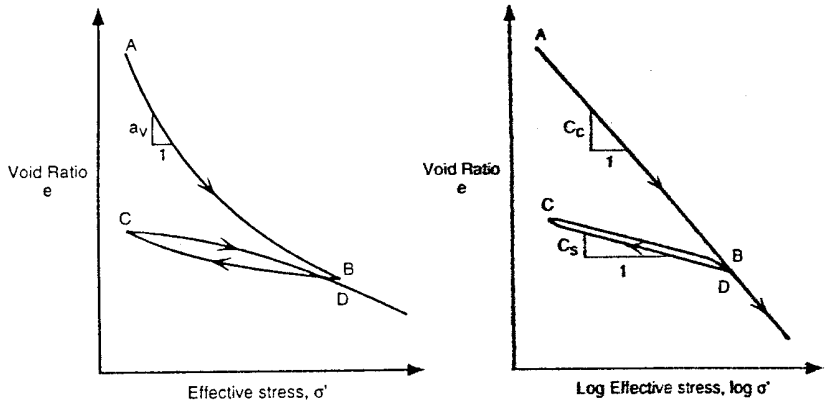

AB = Initial or virgin compression
BC = Rebound or swelling
CD = Recompression

a_v = Coefficient of compressibility = $-de/d\sigma' = -0.434C_c/\sigma'$

m_v = Compressibility = $-a_v/(1+e)$

C_c = Compression index = $-de/d\log\sigma'$ on compression

C_s = Swelling index = $-de/d\log\sigma'$ on swelling

Figure 4.9 Idealized void ratio-effective stress relationships for a compressible soil [3].

$$M_c = \rho_w V_s \left(S a_v \chi' + e \frac{dS}{d\ p} \right). \tag{4.25}$$

By noting that

$$V_s = \frac{V}{1+e} \tag{4.26}$$

and defining $m_c = M_c / V$, the specific fluid mass capacity as

$$m_c = \frac{\rho_w}{1+e} \left(S a_v \chi' + e \frac{dS}{d\ p} \right). \tag{4.27}$$

Substitution of (4.27) into (4.16) yields

$$\frac{1}{V} \int_\Gamma \frac{k \rho_w g}{\mu} \vec{h} \cdot \vec{n} d\Gamma = \frac{1}{1+e} \left(S a_v \chi' + e \frac{dS}{d\ p} \right) \frac{\partial\ p}{\partial t}. \tag{4.28}$$

Here, because the volume element V which is bounded by the surface Γ has a constant solid volume V_S, to be consistent, we may neglect the geometric variation without loss of accuracy, and the material derivative is replaced by the partial derivative.

Furthermore, by letting the elemental volume become arbitrarily small, we may write

$$\frac{\rho_w g}{\mu} \nabla \cdot (k \nabla h) = \frac{1}{1+e} \left(S a_v \chi' + e \frac{dS}{d\ p} \right) \frac{\partial\ p}{\partial t} \tag{4.29}$$

Equation (4.27) is the fundamental equation which describes the behaviour of a deformable medium with incompressible fluid.

The permeability k is a function of S, which is a function of p_w. h is expressed in terms of p_w and the elevation head by (4.15). e is also a function of p_w.

4.2.2 Bentonite Saturated with Water

If we assume that bentonite is saturated with water, i.e., $S = 1$, then, (4.29) reduces to

$$\frac{\rho_w g}{\mu} \nabla \cdot (k \nabla h) = \frac{1}{1+e} \frac{\partial e}{\partial t} \tag{4.30}$$

For a one-dimensional medium, (4.30) can be written as

$$\frac{\rho_w g}{\mu} \frac{\partial}{\partial x} \left(k(e) \frac{\partial h}{\partial x} \right) = \frac{1}{1+e} \frac{\partial e}{\partial t}. \tag{4.31}$$

Substituting (4.15) into (4.31) and assuming the elevation head h_e is constant gives

$$\frac{1}{\mu} \frac{\partial}{\partial x} \left(k(e) \frac{\partial\ p}{\partial x} \right) = \frac{1}{1+e} \frac{\partial e}{\partial t}. \tag{4.32}$$

By the chain rule of derivative and using (4.11) and (4.23)

$$\frac{\partial\ p}{\partial x} = \frac{d\ p}{d\sigma'} \frac{d\sigma'}{de} \frac{\partial e}{\partial x} = (-1)(-\frac{1}{a_v}) \frac{\partial e}{\partial x} = \frac{1}{a_v(e)} \frac{\partial e}{\partial x}. \tag{4.33}$$

Then, (4.32) can be written in terms of e as

$$\frac{1}{\mu}\frac{\partial}{\partial x}\left(\frac{k(e)}{a_v(e)}\frac{\partial e}{\partial x}\right) = \frac{1}{1+e}\frac{\partial e}{\partial t} \tag{4.34}$$

For the e-dependencies of the permeability and the compressibility coefficient, we need measurement for a particular bentonite of interest. However, from many previous measurements, such as illustrated in Figure 4.8 for a_v, and in Figure 4.10 for k, we can express the dependencies as follows.

For the compressibility coefficient, from (4.22), a_v, is expressed as

$$a_v = \frac{C_s}{2.303\sigma'} \tag{4.35}$$

From Figure 4.9, the effective stress can be expressed in terms of e as

$$\sigma' = \sigma_o' \exp\left(-\frac{2.303}{C_s}\left(e - e_o^{\sigma}\right)\right), \tag{4.36}$$

where σ_o' and e_o^{σ} represent an arbitrarily chosen point. With (4.36), (4.35) can be modified as

$$a_v = \frac{C_s}{2.303\sigma_o'} \exp\left(\frac{2.303}{C_s}\left(e - e_o^{\sigma}\right)\right). \tag{4.37}$$

For the permeability, from Figure 4.10, we can derive an expression similar to (4.37) as

$$k = k_o \exp\left(\frac{2.303}{C_k}\left(e - e_o^{k}\right)\right), \tag{4.38}$$

where C_k is the best fitting straight line for the relationship of e versus k.

Substituting (4.37) and (4.38) into (4.34) yields the final form of the governing equation as

$$C\frac{\partial}{\partial x}\left(\exp\left(Ge\right)\frac{\partial e}{\partial x}\right) = \frac{1}{1+e}\frac{\partial e}{\partial t}, \tag{4.39}$$

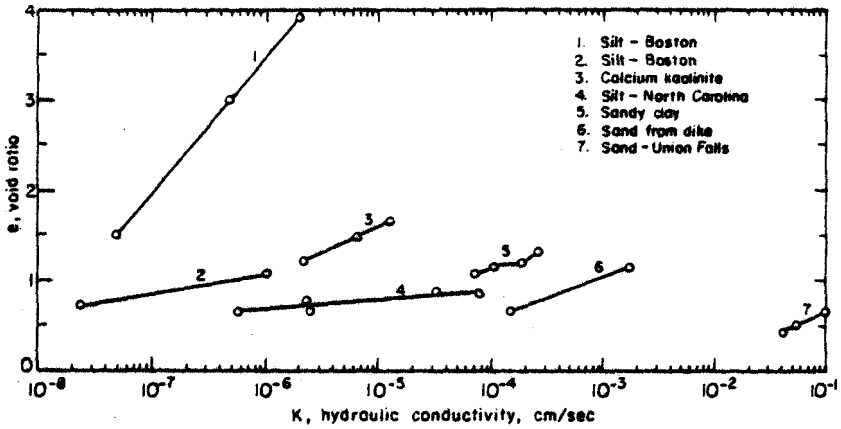

Figure 4.10 Variation of hydraulic conductivity with void ratio for some saturated soils [1].

where C and G are the constants defined as

$$G = 2.303\left(\frac{1}{C_k} - \frac{1}{C_s}\right), \quad C = \frac{2.303\sigma_o' k_o}{\mu C_s}\exp\left[2.303\left(\frac{e_o^\sigma}{C_s} - \frac{e_o^k}{C_k}\right)\right]. \tag{4.40}$$

With the appropriate initial and boundary conditions, (4.39) can be solved for $e(x, t)$. Thus, we can quantitatively estimate the volume expansion of the water-saturated bentonite as a function of time and position.

4.3 REFERENCES FOR CHAPTER 4

[1] T. W. Lambe and R. V. Whitman, *Soil Mechanics*, Wiley, New York (1969).

[2] P. F. Low, Interparticle Forces in Clay Suspensions: Flocculation, Viscous Flow and Swelling, *Proc. 1989 Clay Minerals Soc. Workshop on Rheology of Clay/Water Systems* (1992)

[3] J. K. Mitchell, *Fundamentals of Soil Behaviour*, 2nd ed., Wiley, New York (1993).

[4] A. W. Bishop, The Principle of Effective Stress, *Publ.* 32, Norwegian Geotech. Inst., Oslo, Norway (1960).

[5] K. Terzaghi, The Influence of Elasticity and Permeability on the Swelling of Two-Phase Systems, in J. Alexander (ed.), *Colloid Chemistry*, Vol. III, Chemical Catalog Co., New York, (1931).